Front. Earth Sci. 2018, 12(1): 170–190
https://doi.org/10.1007/s11707-016-0628-6

RESEARCH ARTICLE

The effect of wind on the dispersal of a tropical small river plume

Junpeng ZHAO[1,2], Wenping GONG (✉)[1,2], Jian SHEN[3]

1 School of Marine Sciences, Sun Yat-Sen University, Guangzhou 510275, China
2 Guangdong Provincial Key Laboratory of Marine Resources and Coastal Engineering, Sun Yat-Sen University, Guangzhou 510275, China
3 Virginia Institute of Marine Science, The College of William and Mary, Gloucester Point, VA 23062, USA

Abstract Wanquan River is a small river located in Hainan, a tropical island in China. As the third largest river in Hainan, the river plume plays an important role in the regional terrigenous mass transport, coastal circulation, and the coral reef's ecosystem. Studies have shown that wind forcings significantly influence river plume dynamics. In this study, wind effects on the dispersal of the river plume and freshwater transport were examined numerically using a calibrated, unstructured, finite volume numerical model (FVCOM). Both wind direction and magnitude were determined to influence plume dispersal. Northeasterly (downwelling-favorable) winds drove freshwater down-shelf while southeasterly (onshore) winds drove water up-shelf (in the sense of Kelvin wave propagation) , and were confined near the coast. Southwesterly (upwelling-favorable) and northwesterly (offshore) winds transport more freshwater offshore. The transport flux is decomposed into an advection, a vertical shear, and an oscillatory component. The advection flux dominates the freshwater transport in the coastal area and the vertical shear flux is dominant in the offshore area. For the upwelling-favorable wind, the freshwater transport becomes more controlled by the advection transport with an increase in wind stress, due to enhanced vertical mixing. The relative importance of wind forcing and buoyancy force was investigated. It was found that, when the Wedderburn number is larger than one, the plume was dominated by wind forcing, although the importance of wind varies in different parts of the plume. The water column stratification decreased as a whole under the prevailing southwesterly wind, with the exception of the up-shelf and offshore areas.

Received July 17, 2016; accepted October 23, 2016

E-mail: gongwp@mail.sysu.edu.cn

Keywords small river plume, wind effect, freshwater transport

1 Introduction

A river plume is formed when freshwater from an estuary flows into the coastal ocean. The nature of the dilution pathways and plume structures are critically important as they determine the fate of various constituents, including terrigenous pollutants, sediments, and nutrients, etc. (Yin et al., 1995; Rabalais et al., 2002; Geyer et al., 2004). The spreading of a river plume can be influenced by many external forcings including the Earth's rotation (Garvine, 1999; Huq, 2009), tides (Chao, 1990; Isobe, 2005; Wu et al., 2011), winds (Chao, 1988b; Fong et al., 1997; Fong and Geyer, 2001), and ambient currents (Garcia-Berdeal et al., 2002). The Coriolis force turns the plume towards the down-shelf direction outside the river mouth. The onshore-offshore tidal currents near the estuary mouth can hasten the plume's expansion offshore (Chao, 1990) while the alongshore tidal currents are effective in stabilizing the offshore growth of the river plume and increasing alongshore freshwater transport (Isobe, 2005). On the other hand, the tides can also enhance the vertical mixing and thus limit the expansion of the river plume (Guo and Valle-Levinson, 2007). Ambient alongshore currents can either augment or decrease the plume transport based on the similarities between the direction of each (Fong and Geyer, 2002).

In general, the river buoyant force and tidal mixing are of significance within the estuary and the region adjacent to the river mouth (referred to as near-field), while the wind forcing dominates over the shelf (far-field), where the Coriolis force also becomes important (Hetland, 2005).

Chen and Sanford (2009) and Li and Li (2011) have investigated the net effect of wind on estuarine stratification, which may also be applied to the plume. Wind

influences the transport and mixing of the plume in two ways: wind straining and direct vertical mixing. The direct turbulent mixing always enhances the vertical mixing of the water column and decreases the stratification. The wind straining either increases or decreases the stratification, dependent on the wind direction related to the direction of the plume front and the wind strength. The density difference between the plume and ambient shelf induces a density circulation and stratification, with the diluted water spreading into the surface layer and the dense ocean water compensating into the bottom layer. If the wind direction is the same as that of the extension of the plume, the two layer circulation increases at the plume front, thus reinforcing the stratification and enhancing the transport of the plume. Alternatively, the situation is reversed when the wind is opposite to the buoyancy-driven circulation. The wind-dominated shear flow then favors the steepening of the isopycnals and reduces the stratification and freshwater transport. The competition between wind straining and wind mixing decides the mixing and transport of the plume.

In general, an upwelling-favorable wind enhances the plume's offshore transport. It widens plume dispersal and decreases the thickness of buoyant outflows. As the cross-shelf density gradient weakens, the plume eventually separates from the coast and moves offshore (Fong and Geyer, 2001). For the downwelling-favorable winds, the onshore Ekman transport causes buoyant water to flow against the coast, which compresses the plume and steepens the pycnocline; thus, the plume becomes narrow and thick (Rennie et al., 1999; Johnson et al., 2001). Besides the cross-shelf transport, upwelling-favorable winds arrest the down-shelf buoyant-driven flow, reversing the flow direction, while downwelling-favorable winds tend to accelerate the down-shelf transport (Simpson, 1997).

The effects of onshore and offshore winds on river plume have been studied based on observations and numerical modeling (Chao, 1988b; Choi and Wilkin, 2007). However, the complex mechanisms for controlling plume size and spreading under the interactions of internal mixing and external wind forcing from different directions are not well understood. Jurisa and Chant (2013) examined the response of a buoyant river plume to offshore wind stress based on an idealized model. They found that the stable offshore position of the plume can be described by the ratio of the outflow Froude number (the ratio of the average outflow velocity to the internal wave speed at the mouth of the estuary) and the plume Froude number (the ratio of the plume-averaged velocity and internal wave speed at a down-shelf transect). The salinity structure in the plume is a balance between the cross-shelf advection and the down-shelf transport.

The effect of winds on the large river plume has been studied widely, revealing significant influences on the coastal hydrography over an extensive area (Whitney and Garvine, 2005; Lentz and Largier, 2006; Moffat and Lentz, 2012). Many of these studies have focused on the dynamics of large river plumes in the northern South China Sea (NSCS) (Shu et al., 2011; Pan et al., 2014; Shu et al., 2014). Comparatively, fewer studies have investigated low-latitude tropical small river plumes, where the effects on coastal dynamics are more local in extent and lower in intensity. Small river plumes are dissimilar to larger plumes in that they are typically connected to the ocean by an estuary and event-driven by a rain storm. The extent of the plume is limited, and the dynamics are more controlled by outflow jets from the mouth of the river. Such examples include the Maipo River plume in Chile (Piñones et al., 2005), Mooloolah estuary river plume, Australian East Coast (Gaston et al., 2006), Southern California small river plumes (Warrick et al., 2007), Kaneohe Stream, Hawaii (Ostrander et al., 2008), Tet River in Lion Bay, Mediterranean (Bourrin et al., 2008), and Berau River plume, Indonesia (Tarya et al., 2015). Ostrander et al. (2008) indicated that the spatial variation of small freshwater plumes is primarily determined by atmosphere forcing. Geyer et al. (2000) showed that for small rivers, freshet events lived mainly at the same time scales as the meteorological events that supply the precipitation. Thus the wind forcing during the brief period of high flow may determine the structure of small river plumes.

In this investigation, we studied the Wanquan River plume, a small river located in the tropical island of Hainan, China. Reasons for choosing the study site include: (i) the estuary is characterized by a small tidal range, and the river plume is mostly surface-advected, making it an ideal site for studying the wind effect; (ii) the narrow mouth connecting the estuary and the coastal ocean generates a jet outflow, which largely controls the spreading of the plume; from the perspective of plume classification, the plume can be considered as supercritical (Chao, 1988a); (iii) the outflow is at a large angle ($>90°$) to the coast, which may initially affect the alongshore momentum; and (iv) the river discharge and wind in the study site experience distinct seasonal variation, with the river discharge being largest by runoff during storm events in summer. Meanwhile, a mild southwesterly East Asian monsoon prevails in summer, with occasional typhoons.

As the tides are weak in this region, and the ambient current is relatively insignificant (as shown later), the wind becomes the main external forcing for the spreading of the plume. This study focuses on the wind effect on the dispersal of the Wanquan River plume. A numerical model was used to study the spatial salinity and current structure of the plume responding to winds of different magnitudes and directions. The aims of this study are: 1) to examine the effect of winds on the dispersal of the river plume, such as the horizontal extent and the freshwater penetration depth of the river plume; and 2) to investigate the transport mechanisms of the freshwater impacted by the winds.

This paper is organized as follows: The study site and

methodology are described in Section 2. Section 3 reports the model validation and designs of numerical experiments. In Section 4, the model results are presented and analyzed. The freshwater transport flux is decomposed and analyzed consequently in Section 5. Finally, discussion and conclusions are provided in Sections 6 and 7, respectively.

2 Study area and methodology

2.1 Introduction to the Wanquan River Estuary

The Wanquan River Estuary is located in the eastern portion of Hainan Island, the southernmost tropical island in China. Discharge from the Wanquan River enters the South China Sea through Boao, a small beautiful town famed as "the heaven small town" (Fig. 1). The estuary is composed of a sinuous river channel and many islands near the river mouth. The estuary is separated from the coastal sea by an extended sand barrier and connects to the ocean by a narrow mouth. The mouth width varies from 60 m to 500 m, determined by the deluge, storm surge, and strong waves. The longshore littoral transport is estimated to be around 10^5 m^3 per year with a dominant northward direction, causing the mouth of the estuary to shift frequently. The bathymetry outside the mouth is asymmetric in the alongshore direction. The distance offshore of the 30-m isobath is greater in the northern than in the southern area of the estuary. As a result, the northern part outside the estuary is shallower than the southern part.

The climate in the region is largely controlled by the East Asian monsoon. There is a distinct variation in rainfall between dry (winter) and wet (summer) seasons. About half of the annual precipitation falls in summer from August to October, while only 13%–16% in winter and spring. The rainfall in the flood season is mostly induced by storms and typhoons. According to the monthly averaged data from 1998 and 2007 at the Jiaji hydrologic station (nearest station upstream of the river mouth), the largest discharge (approximately 360 $m^3 \cdot s^{-1}$) occurs in October, and the smallest (58 $m^3 \cdot s^{-1}$) occurs in March (Fig. 2). The tides in the area are characterized as mixed diurnal tides with micro-tidal range. The mean tidal range

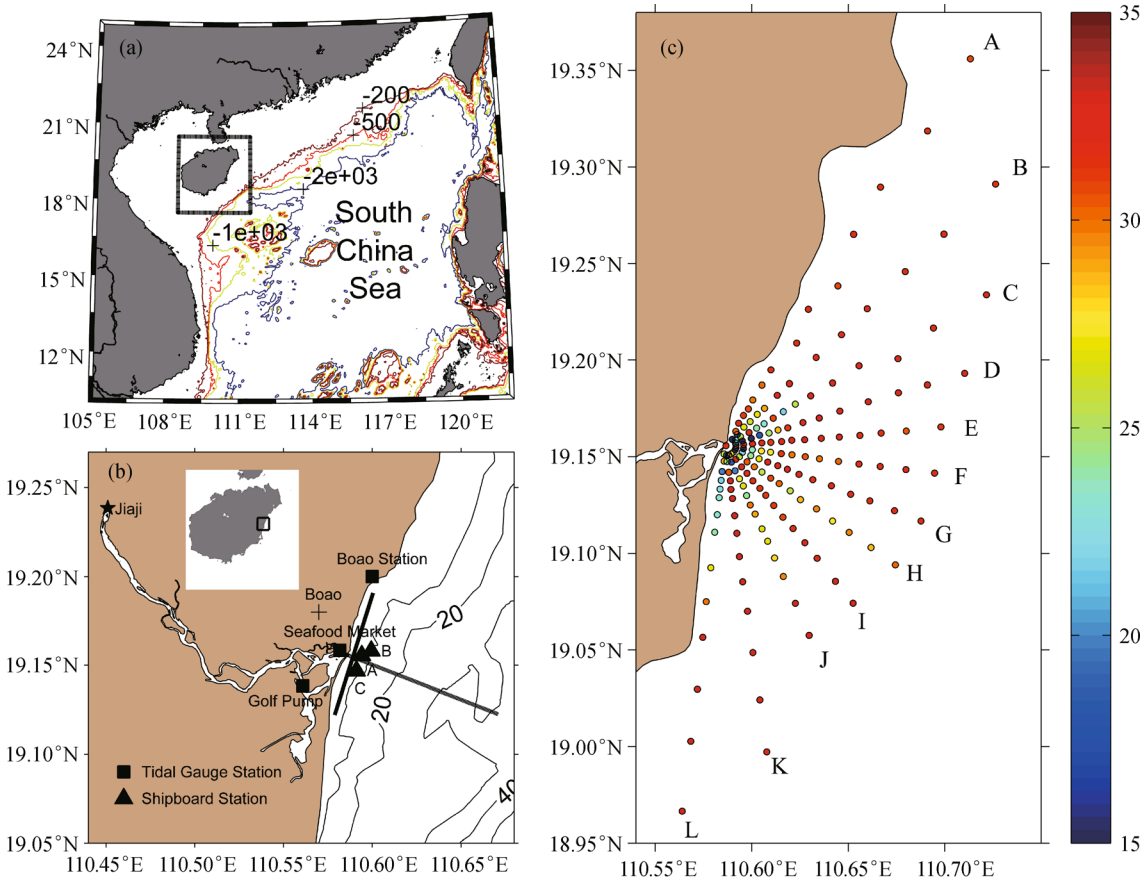

Fig. 1 Study area and the *in-situ* observation stations. In panel (b), the isobaths are included with an interval of 10 m. The filled squares represent the tidal gauge stations, and the filled triangles represent the shipboard survey stations in summer, 2012. The solid and dotted lines are the alongshore transect and cross-shelf transect, respectively. The filled cycles in panel (c) indicate the locations of underway stations, and the color denotes the surface salinity measured.

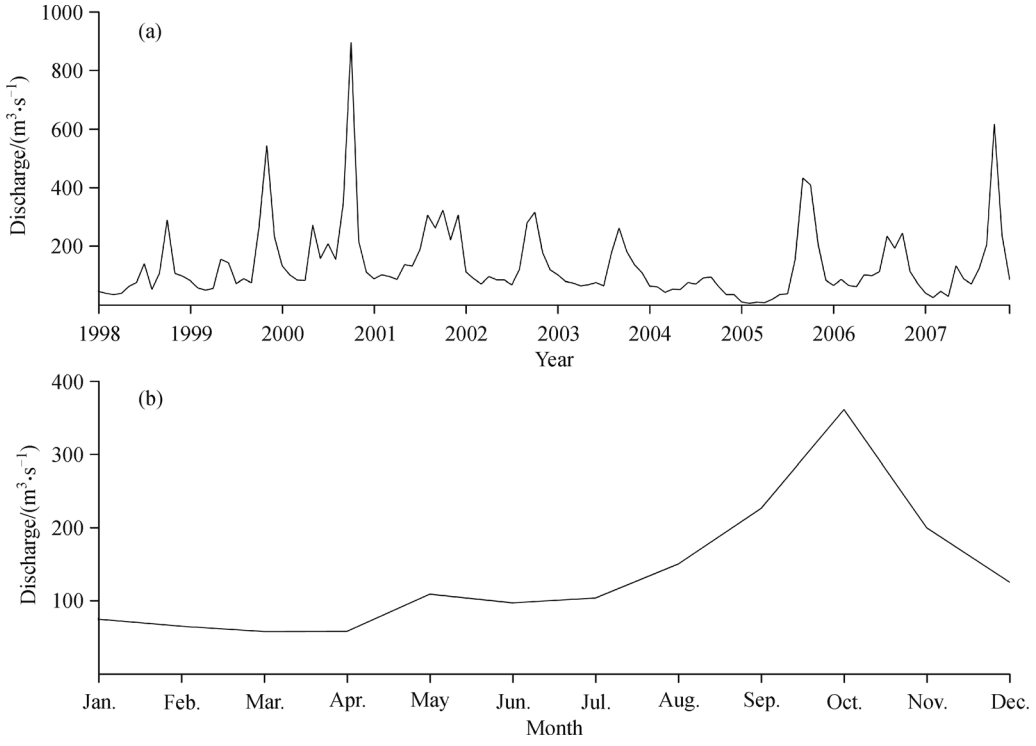

Fig. 2 (a) The monthly measured discharge from 1998 to 2007 and (b) the monthly averaged discharge at the Jiaji hydrologic station.

is 0.7–0.8 m, and the spring tidal range is 1.32–1.57 m. A large tidal range occurs when diurnal tides are dominant, and a small range occurs when semi-diurnal tides are dominant. Northerly winds prevail during the winter monsoon season while southerly winds prevail during the summer monsoon season. The strongest monthly mean wind occurs in April with a speed of 3.1 $m \cdot s^{-1}$. The area is frequently exposed to tropical storms and typhoons in the summer, which may bring torrential rainfall and strong winds. The strongest observed wind during a typhoon is approximately 28.0 $m \cdot s^{-1}$.

2.2 Methodology

In situ measurements were carried out in August 2012 after the Typhoon 'Qide' made landfall on Hainan Island, during which time the peak river discharge was more than 350 $m^3 \cdot s^{-1}$. The field survey was implemented from August 21–26, 2012, encompassing a neap tide (August 21–22, 2012) and a spring tide (August 25–26, 2012). The observations were conducted using a shipboard profile and an underway survey. The shipboard profile measured the time series of water elevation, vertical profiles of salinity, and temperature and turbidity every hour for a diurnal cycle (25 hours) at three stations outside the mouth simultaneously during a neap tide and a spring tide, respectively (Fig. 1(b)). The underway survey collected vertical profiles of salinity, temperature, and turbidity from 168 sampling stations in 12 transects radiating from the estuary mouth on August 21 and 24, 2012 (Fig. 1(c)) by 3 fishing boats. Transects A, E, and I were measured from the mouth towards the offshore while transects C, G, and K were measured from the offshore towards the mouth on August 21, 2012; Transects B, F, and J were measured from the mouth towards the offshore, while transects D, H, and L were measured from the offshore towards the mouth on August 24, 2012. Due to the logistical limitation and rough sea state, the spatiotemporal coverage of the measurement was not very extensive.

To compensate for the insufficiency of the coverage of observations in both time and space, the finite volume coastal ocean model (FVCOM) was used to implement the numerical simulation of the Wanquan River plume system. FVCOM is an unstructured-grid, finite-volume, 3-D coastal ocean model (Chen et al., 2003). The finite-volume approach for solving the primitive Navier-Stokes equations combines the advantages of finite-element methods for flexibility in handling complex shorelines with the ability of finite difference methods to handle simple discrete structures; thus, ensuring mass conservation at both the single element and over the entire mesh domain and providing computational efficiency through a variable mesh size. FVCOM has been used extensively in many plume simulations (Chen et al., 2008; Wang et al., 2010; Ge et al., 2015).

In order to minimize the inaccuracy of boundary specifications, the computational domain covers the entire east portion of Hainan Island and extends from the mouth

to the 175-m isobath (Fig. 3). The model is discretized with a horizontal resolution of ~30–50 m inside the estuary and near the mouth and can resolve the strong bathymetric gradient. The resolution becomes coarser with up to 3–4 km near the open boundary. A total of 41 uniform sigma levels are used in the vertical, which corresponds to a vertical resolution of 0.25 m or less near the mouth for better simulation of the thin plume in the surface layer. The total number of triangular elements and nodes is 53,472 and 27,911, respectively. The time steps used for the external mode and internal model are 0.5 s and 3.0 s, respectively. The model uses the Smagorinsky scheme for horizontal mixing and the MY-2.5 scheme for vertical mixing. The background turbulent diffusivity is set to 3×10^{-6} $m^2\cdot s^{-1}$. The bathymetry data in the estuary and near the mouth were extracted from the nautical chart of Boao Port, and water depths in the coastal ocean and continental shelf were obtained from the global ETOPO1 bathymetry data set (http://www.ngdc.noaa.gov/mgg/global/).

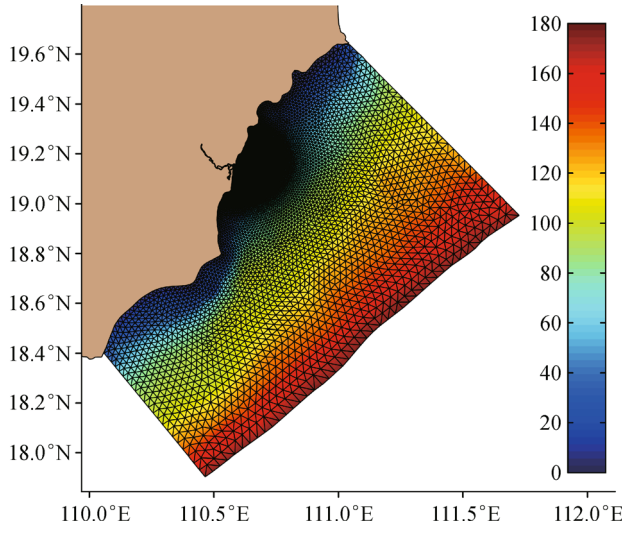

Fig. 3 The model domain and bathymetry (m).

The model was forced by river discharge, tides, wind, and ambient current. The barotropic effects of remote wind and ambient current can be resolved by adding a residual water level at the open boundary. Freshwater discharge data was collected upstream from the Jiaji Hydrologic Station in August 2012 from the daily river inflow. The open boundary was specified by tidal elevation and residual water level. The time series of tidal elevation was predicted by T_tide Matlab package with the tidal amplitudes and phases of eight major tidal constituents: S_2, M_2, N_2, K_2, K_1, P_1, O_1, and Q_1. These harmonics were extracted from a 1/30° resolution China Seas solution (Egbert and Erofeeva, 2002). Given no time series of observed wind data exist for this area, the 10 m-above-ground wind data were obtained from the National Centers for Environmental Prediction (NCEP) Climate Forecast System (http://rda.ucar.edu/datasets/ds094.1/) (Saha et al., 2014), with a temporal resolution of 1 hour and a spatial resolution of ~0.2 degrees. The interpolated wind field in the modeled domain is nearly uniform due its small scaled size and low resolution of wind data. The residual water level and salinity at the open boundary were retrieved from HYCOM + NCODA Global 1/12° Analysis data (GLBa0.08).

Since temperature variations are small throughout the shallow Boao region, a constant temperature of 29°C in the entire domain was used. The calculation of density is based on the assumption that it is a linear function varying solely with salinity: $\Delta\rho = r_\beta \times \Delta S$, where the saline contraction coefficient is $r_\beta = 0.757\ kg\cdot m^{-3}\cdot psu^{-1}$. The Coriolis forcing was taken as a constant at a latitude of 19°N. The model was initialized with a salinity field interpolated from HYCOM + NCODA Global 1/12°Analysis data (GLBa0.08) with the exception of the coastal area and outside the mouth where the salinity was interpolated from the underway profile data. In the Wanquan freshwater estuary, the salinity was set as zero. The initial flow was at rest, and the sea level was zero. After testing, the model spin-up time was set as 10 days.

To examine the effect of wind on freshwater dispersal and storage, we calculated the equivalent depth of the freshwater d_{fw}, which is defined as (Choi and Wilkin, 2007):

$$d_{fw} = \int_{-h}^{\eta} \left(1 - \frac{S}{S_0}\right) \mathrm{d}z, \tag{1}$$

where S_0 is the ocean salinity (34.5 psu here), S is the salinity at the model cell, η is the water level, and h is the depth at the bottom of the plume. Thus d_{fw} represents the total freshwater thickness in the water column.

To investigate the freshwater transport of the plume further, the total depth-integrated freshwater flux per unit width can be decomposed into three terms: advection, vertical shear, and oscillatory:

$$F_f = \langle Q \rangle \langle \overline{\delta_f} \rangle + \langle h\overline{u'\delta_f'} \rangle + \langle \tilde{Q}\tilde{\delta}_f \rangle, \tag{2}$$

where F_f is the freshwater flux. Q is the total rate of flow and $Q = h\bar{u}$. $\delta_f = \dfrac{S_0 - S}{S_0}$ is the freshwater fraction of the waters. The depth average is denoted by the overbar, while the primed variables are the deviation from the depth-averaged values. Angle brackets indicate averaging over eight days and tildes denote time variance. The first term on the right-hand side of Eq. (2) is the depth-mean flow induced advection transport, which is induced by the estuarine outflow and the wind-driven current. The second term is the vertical shear transport, caused by the correlation between the depth variation of the flow and salinity. The vertical shear transport is closely related to the stratification of the water column. Since tide is not

included in the following experiments, the third term (oscillatory transport) comes from the difference in responses of velocity and salinity to the wind.

3 Model validation and numerical experiments

The data collected at the tidal gauging stations and *in situ* observations were used to validate the model. The station locations are shown in Fig. 1(b) and Fig. 1(c). The model was verified for water level and salinity at the stations.

The results of surface elevation calibration are shown in Fig. 4. The Seafood Market and Golf Pump stations are located in the Wanquan estuary, while the Boao gauging station is located along the coastline. The water level at Seafood Market and Golf Pump stations was collected in May 2009; thus the validation results at both stations were simulated using the same mesh grids, but the external forcings, in 2009. The model generally reproduced the tidal fluctuations. At the Seafood Market station, the simulated tidal range was a little larger than the observations, and the simulated low tide was about one hour ahead of the measured tide. On May 14th and 15th, 2009, there was a water withdrawal at the Golf Pump station, resulting in a dramatic drop in the water level. The model did not reflect such an event, resulting in a large discrepancy during this period.

The modeled time series of salinity profiles at the mooring stations were compared with the observation data (Fig. 5). The model results show similarities in the patterns of tidal variation in the vertical salinity profiles and the observations during the neap tide, but the modeled surface salinity is lower than the observations. During the spring tide, the sea condition was harsh with strong waves and heavy rainfall. As precipitation was not included in our model, the model results seem saltier than the observations.

To further quantify the accuracy of model results, we calculated the correlation coefficient (r), average absolute difference (*AAD*), root mean square error (*RMSE*), and a skill assessment parameter (Warner et al., 2005; Ralston et al., 2010; Zhang and Sheng, 2013; Pan et al., 2014).

r measures the linear relationship between the model and the observations:

$$r=\frac{\sum_{i=1}^{N}\left(X_{\mathrm{mod}}-\overline{X}_{\mathrm{mod}}\right)\left(X_{\mathrm{obs}}-\overline{X}_{\mathrm{obs}}\right)}{\left[\sum_{i=1}^{N}\left(X_{\mathrm{mod}}-\overline{X}_{\mathrm{mod}}\right)^{2}\sum_{i=1}^{N}\left(X_{\mathrm{obs}}-\overline{X}_{\mathrm{obs}}\right)^{2}\right]^{1/2}}. \quad (3)$$

Additionally, *AAD* between the model and observations is calculated as

$$AAD=\frac{1}{N}\sum_{1}^{N}\left|X_{\mathrm{obs}}-X_{\mathrm{mod}}\right|, \quad (4)$$

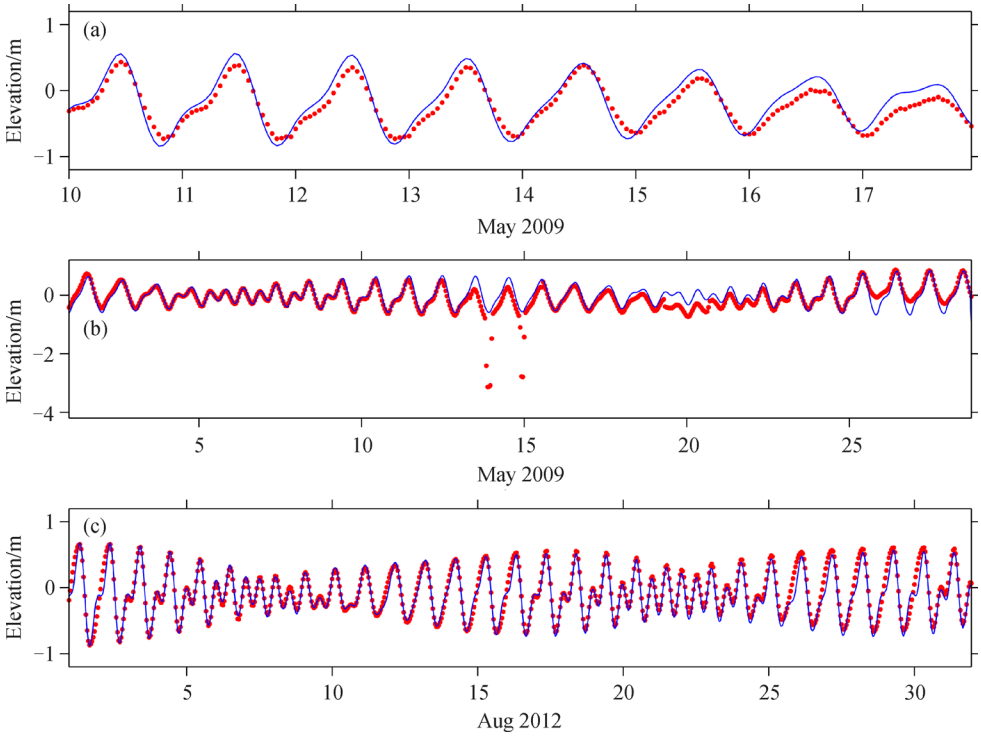

Fig. 4 Comparison of observed (dotted lines) and modeled (solid lines) water elevations at three tidal gauge locations.

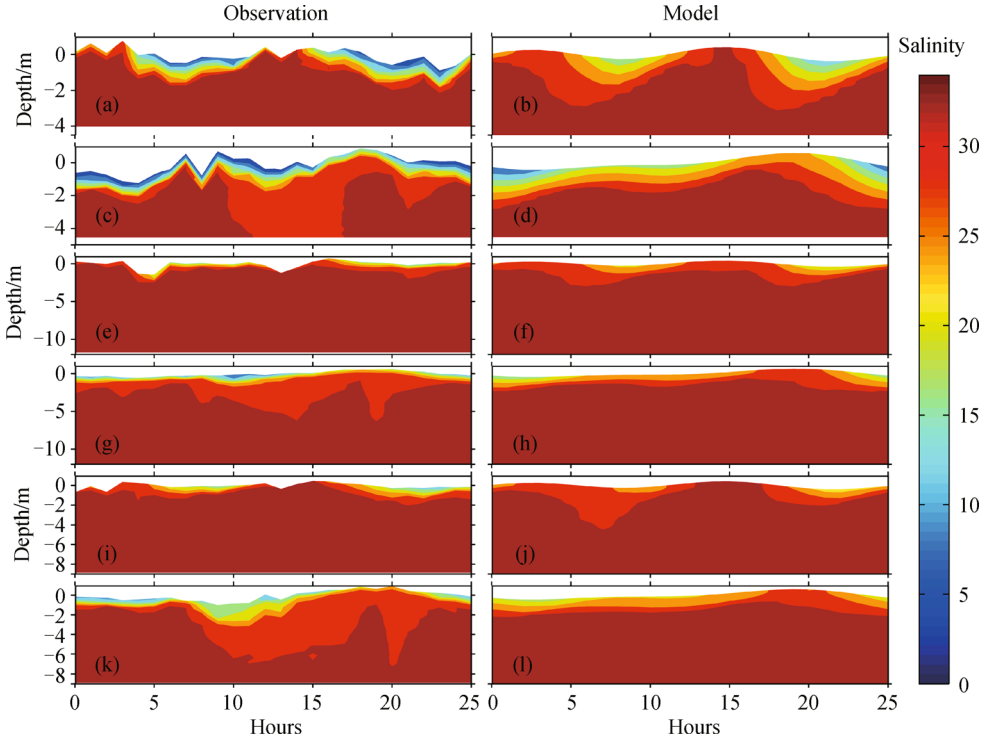

Fig. 5 Comparison of observed and modeled salinity profiles.

and *RMSE* is calculated as

$$RMSE = \left[\frac{1}{N}\sum_{1}^{N}(X_{\mathrm{mod}} - X_{\mathrm{obs}})^2\right]^{1/2}. \quad (5)$$

Another skill assessment parameter (*skill*) is used to quantify the accuracy of the model results, defined as

$$skill = 1 - \frac{\sum_{1}^{N}|X_{\mathrm{mod}} - X_{\mathrm{obs}}|^2}{\sum_{1}^{N}\left(|X_{\mathrm{mod}} - \overline{X_{\mathrm{obs}}}| + |X_{\mathrm{obs}} - \overline{X_{\mathrm{obs}}}|\right)^2}, \quad (6)$$

where X is the variable of interest and $\overline{X}$ is the time mean.

The parameters of the elevation at the three tidal gauging stations and the surface salinity at three shipboard stations are listed in Table 1, showing that the model generally captures the spatiotemporal variations of the elevation and salinity. At the three tidal gauging stations, r values are larger than 0.85, and *skill* values are larger than 0.9, suggesting a good correlation between model and observation results. *AAD* and *RMSE* are larger in the estuary than in the coast, which is due to the complex geometry and bathymetry in the estuary.

The model also adequately represents phasing of the surface salinity during the neap and spring tidal cycles at Stations A and C, where r values are larger than 0.7 and *skill* values are larger than 0.65, although the correlations at Station B are relatively weaker ($r < 0.45$ and *skill* < 0.65). *AAD* and *RMSE* show some difference in salinity between model and observations. Note that we mainly focus on the dynamics of the plume and have no intention to accurately reproduce it. The model shows a reasonable skill.

The comparison of the surface salinity between the model result and observed values from the underway cruise is shown in Fig. 6. The modeling surface salinity is extracted according to the location and time of the cruise

Table 1 r, *AAD*, *RMSE*, and Skill Assessment Parameter (*skill*) for modeled elevation and surface salinity

Parameter	Elevation			Salinity					
	Golf Pump[a)]	Seafood Market	Boao	A, neap	A, spring	B, neap	B, spring	C, neap	C, spring
r	0.85	0.96	0.97	0.81	0.82	0.44	0.31	0.7	0.79
AAD	0.12	0.12	0.06	5.37	5.45	2.15	2.99	2.81	4.08
RMSE	0.14	0.13	0.08	5.75	5.76	2.64	4.12	3.29	4.68
skill	0.92	0.96	0.98	0.76	0.74	0.65	0.58	0.72	0.65

[a)] The data during observation at the Golf Pump Station are discarded when calculated the parameters.

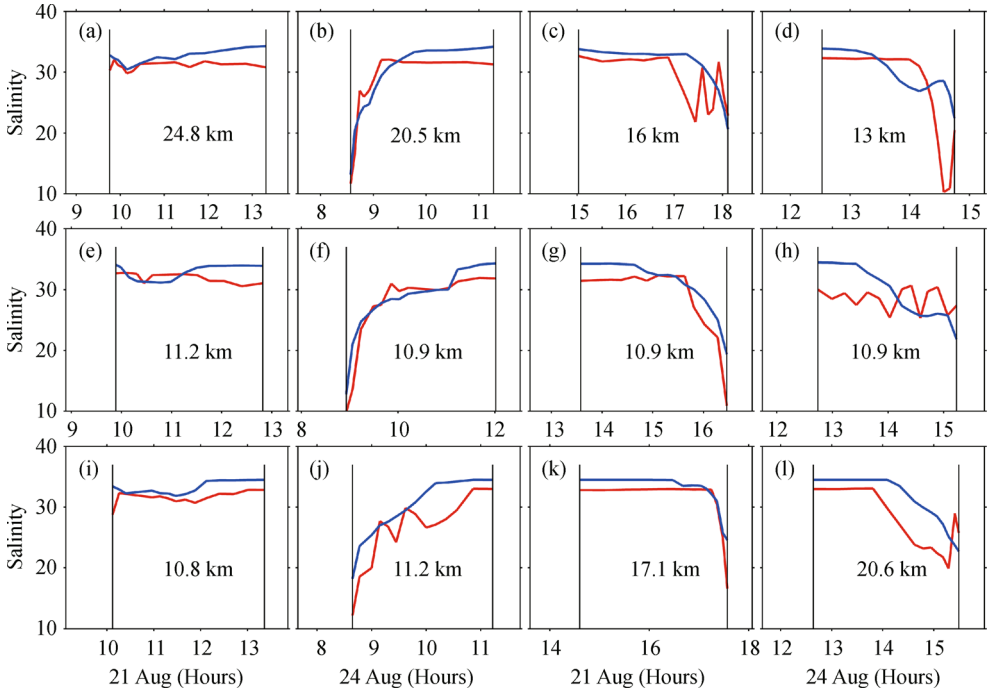

Fig. 6 Comparison of surface salinity from model simulation (blue lines) and underway observation (red lines) for the 12 sections.

transects. It indicates that the modeled surface salinities generally agree with the cruise measurements. The discrepancy may be due to the wave effect during the cruise that is not considered in the model as well as the difference in bathymetry between the observations and predictions by the model.

We tested the effects of remote wind and the ambient current by including and excluding wind forcing at the open boundaries. The results showed little difference in the plume area extent and structure between these two experiments, suggesting the dynamics of the Wanquan River plume are mainly controlled by local forcings. This is due to the fact that the Wanquan River plume is mostly confined in the nearshore area where the ambient current is rather weak (on the order of 1 $cm \cdot s^{-1}$). Thus, the slow variance in the large-scale ambient shelf circulation and the currents associated with the shelf waves induced by remote winds were excluded from the simulation. With respect to local forcings, the tide is microtidal, the current is weak (see the discussion section), and the wind is the dominant driving force. Therefore, we focus on the wind effect on the plume dispersal per following. Eight numerical experiments were designed, each configured with only river outflow and different wind magnitudes and directions. The southwesterly wind is predominant in the summer when the discharge is relatively large. Additionally, earlier studies suggest that upwelling-favorable wind forcing is the primary mechanism for the offshore dispersal of many buoyant coastal plumes (Rennie et al., 1999; Sanders and Garvine, 2001). We focus on the impact of this southwesterly wind on the river plume and freshwater transport with different wind stresses. As the monthly mean wind in this area is 3.1 $m \cdot s^{-1}$, we incorporated four different wind velocities: (1, 3, 5, and 10) $m \cdot s^{-1}$. These wind speeds correspond to the wind stresses of (0.0012, 0.0108, 0.03, and 0.12) Pa, respectively (Large and Pond, 1981). The other three wind directions, namely northeasterly, northwesterly, and southeasterly with a velocity of 5 $m \cdot s^{-1}$, are also simulated to show the effect of wind direction, although their occurrence is not as frequently as the southwesterly wind. A base simulation was conducted without wind. We initially ran the model for 16 days with a constant river discharge of 200 $m^3 \cdot s^{-1}$ (0 psu) in the absence of winds. This discharge is the mean river discharge in the flood season. The fresh water is discharged into a homogeneous shelf. The model result was then stored and used as the initial condition for the subsequent eight experiments. The same river discharge and the wind forcings from different directions with varying magnitudes were then specified from the 17th day to examine the plume response to various wind forcings.

In this study, the plume boundary is defined by the 34.0 psu isohaline based on the surface (1-m thickness) salinity, and the mean plume thickness is estimated on the mean depth of the 34.0 psu isohaline. For all cases considered, this isohaline is a reasonable proxy for the thickness of the buoyancy anomaly and the depth of penetration of the surface wind stress.

4 Model results

Before presenting the model results, the Kelvin number and the internal Froud number at the river mouth were computed. The Kelvin number is defined as the ratio of the width of a river estuary mouth to the internal Rossby deformation radius, and indicates the dynamic scale of a river plume (Geyer et al., 2000; Huq, 2009). Based on the survey of the stratification at the mouth, the internal Rossby deformation was calculated as ~8.7 km, with the width of the mouth at ~0.3 km, resulting in a small Kelvin number of ~0.03, which implies that the inertial effects at the mouth are more important relative to the rotation. In the parameter space in Huq (2009), this suggests that the plume favors the formation of an anticyclonic circulation bulge. Based on the measured ebb velocity at Shipboard Station A, which is close to the mouth, the internal Froude number (the ratio of the outflow velocity and internal wave speed) was about 1.21 at the mouth (supercritical), indicating the dynamics were strongly influenced by the momentum input from the river (Garvine, 1995).

Our model results indicate that the plume extension reaches a quasi-steady state approximately six days after the winds of different directions and magnitudes have acted on the sea surface (not shown). Here we compare the status of the plume after eight days to illustrate the plume evolution process.

4.1 Base condition

The base condition is the simulation without wind. Figure 7 shows the distribution of surface salinity and freshwater thickness as the initial condition and after eight days of the simulation. It can be seen that initially, a bulge exists off the mouth consisting of a large eddy rotating anticyclonically. The bulge impinges upon the coast at 19.05°N and leads to the split of the buoyant current. A portion of freshwater recirculates into the bulge, while the remaining portion flows down-shelf and becomes a coastal current (Figs. 7(a) and 7(c)). The bulge grows continuously in time, and the impinging point moves to 18.95°N after 8 days (Figs. 7(b) and 7(d)), accompanied by the extension of the bulge.

For the unforced river plume, the shape of the bulge and the freshwater transport in the coastal current is found to be highly dependent on the Rossby number of outflow, $Ro = u_r/(fw)$, where Ro is the Rossby number, u_r the outflow velocity, f the Coriolis parameter, and w the width of the river mouth (Fong and Geyer, 2002; Horner-Devine et al., 2006). Higher Rossby number discharge results in a more circular bulge and less coastal current transport. In the base condition, the Rossby number is 1.53, indicating a greater reduction in freshwater in the coastal current compared with the discharge source (Fong and Geyer, 2002). For the base condition, the freshwater transport in the coastal current (measured at 18.85°N) is approximately 25% of the freshwater input by the river. Another factor impacting the plume transport is the coastline geometry. Avicola and Huq (2003) and Whitehead (1985) suggested that, if the exit angle is less than 90°, more freshwater away from the river mouth will be transported into the coastal current and vice versa. At the mouth of the Wanquan estuary, the exit angle is greater than 90° (directly up-shelf). This situation increases the offshore expansion and the importance of the Coriolis term in the alongshore momentum balance (Nof and Pichevin, 2001), and decreases the proportion of freshwater flowing into the down-shelf coastal current.

4.2 The plume extension under different wind forcings

4.2.1 Effect of wind direction

Moderate (5 $m \cdot s^{-1}$) winds from varied directions are applied in the experiments to examine the responses of the plume. Obviously, the current field and plume structure are different in each run (Fig. 8). A southwesterly wind drives the northeastward surface flow in shallow coastal areas. When the water depth is greater than 60 m, the flow turns southeastward due to the Coriolis force (Figs. 8(a) and 8(e)). The bulge presented in the base case completely disappears. The surface water's low salinity extends towards the northeast and separates from the coast. The freshwater is mainly distributed in the northeast direction and offshore of the mouth. When the wind is northeasterly (Figs. 8(b) and 8(f)), the surface flows to the southwest in the offshore area, but along the coastline. The plume is confined near the mouth. The freshwater is transported in the narrow, coastal current jet, far from the mouth, with a depth much greater than that of the southwesterly wind.

For the northwesterly wind (Figs. 8(c) and 8(g)), the jetlike flow rushes out of the mouth towards the south as it is constrained by the wind. The freshwater band is much wider than that of the northeasterly wind.

The southeasterly wind effectively pushes the freshwater up-shelf of the mouth (Figs. 8(d) and 8(h)). The surface flow is relatively weak compared to those of the other three wind scenarios, and flows to the northwest in the offshore area along the coastline. As a result, most of the freshwater is stored in the shallow up-shelf area.

The vertical profiles of the current and salinity in the cross-shelf and alongshore transects are also examined (Fig. 9). The locations of the sections are shown in Fig. 1 (b). Under different wind directions, the isohalines tilt in the plumes, suggesting that a wind velocity of 5 $m \cdot s^{-1}$ can lead to considerable vertical mixing. Near the mouth, the current directions are offshore in the upper layer, while a compensated undercurrent exists in the bottom layer. In the alongshore transects, the salinity distribution is approximately symmetrical near the mouth (3.2–4.5 km), indicat-

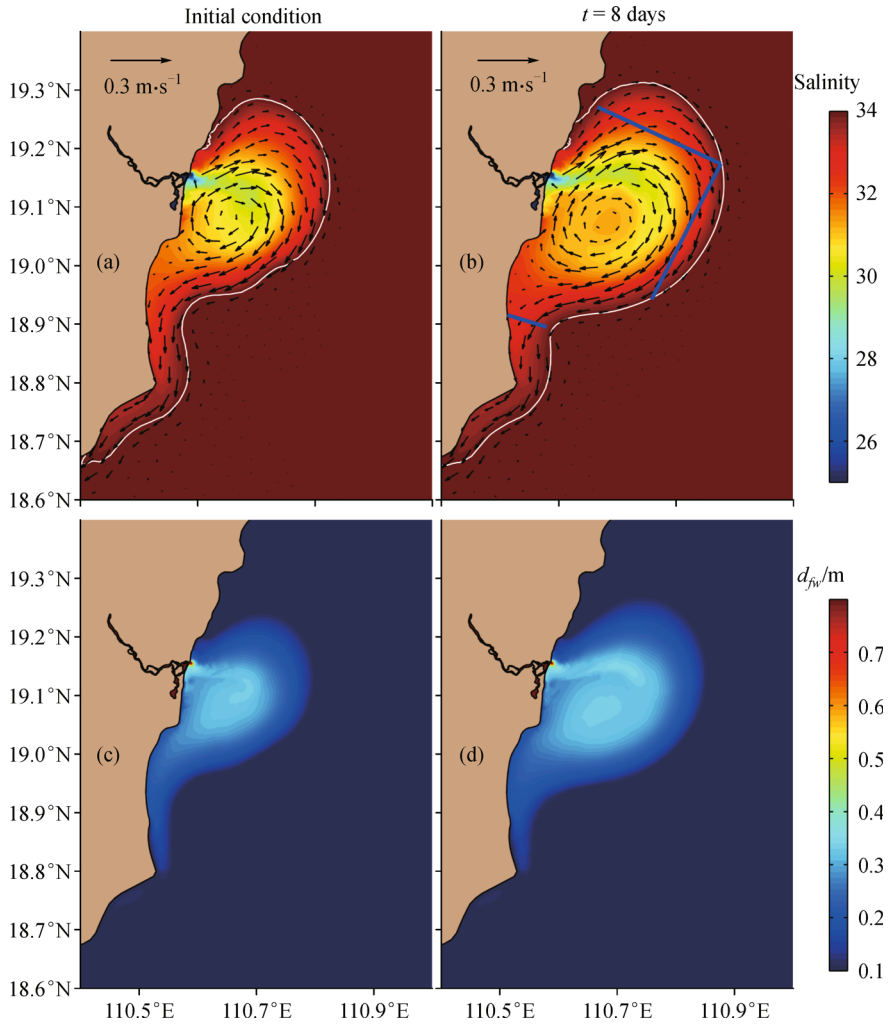

Fig. 7 Surface salinity and flow (a, c) and freshwater depth (b, d) for the initial condition and after 8 days of the simulation without wind. The white lines in the upper panel represent the 34.0-psu isohaline. The blue lines in (b) indicate the sections for calculating the Wedderburn number and PEA.

ing that the plume dispersal near the mouth is mainly controlled by the outflow buoyancy. This is consistent with the supercritical condition at the mouth.

The plume can reach a maximum offshore distance under the northwesterly wind, yet a minimal distance with a northeasterly wind. The alongshore distance is greater under the southeasterly wind than under the southwesterly wind. Under the southwesterly wind, the flow is offshore and up-shelf. An upwelling flow develops beneath the plume while a downwelling flow develops at the offshore boundary of the plume. The alongshore velocity is larger offshore than in the near-field. The vertical stratification is greater in the up-shelf side of the mouth in the along-shore direction and decreases toward the offshore direction (Figs. 9(a) and 9(b)). Alternatively, the flow is down-shelf and the horizontal shear is small under a northeasterly wind. In addition, the vertical velocity is opposite to that of the southwesterly wind condition, with a downwelling flow beneath the plume and an upwelling flow offshore the plume. The salinity in the plume is relatively uniform in the alongshore and cross-shelf sections (Figs. 9(c) and 9(d)). Under the alongshore winds, the vertical shear is larger where there is stratification, as the kinetic energy is inhibited by the deeper penetration and is smaller in the well-mixed area (Figs. 9(b) and 9(d)). The northwesterly wind enhances the offshore flow and entrains the bottom salt water upward. The flow in the alongshore direction is mainly down-shelf in the plume, while up-shelf beneath the plume. Salinity stratification is obvious in the cross-shelf section. By contrast, salinity stratification in the alongshore direction is smaller (Figs. 9(e) and 9(f)). The onshore southeasterly wind impedes the freshwater spreading offshore, thus forcing it to spread alongshore, primarily to the northeast due to Ekman effect. The convergence between buoyancy-driven outflow and south-easterly wind-induced flow leads to a downwelling flow at the offshore boundary of the plume. In the plume, the flow is down-shelf near the mouth, but up-shelf in the offshore

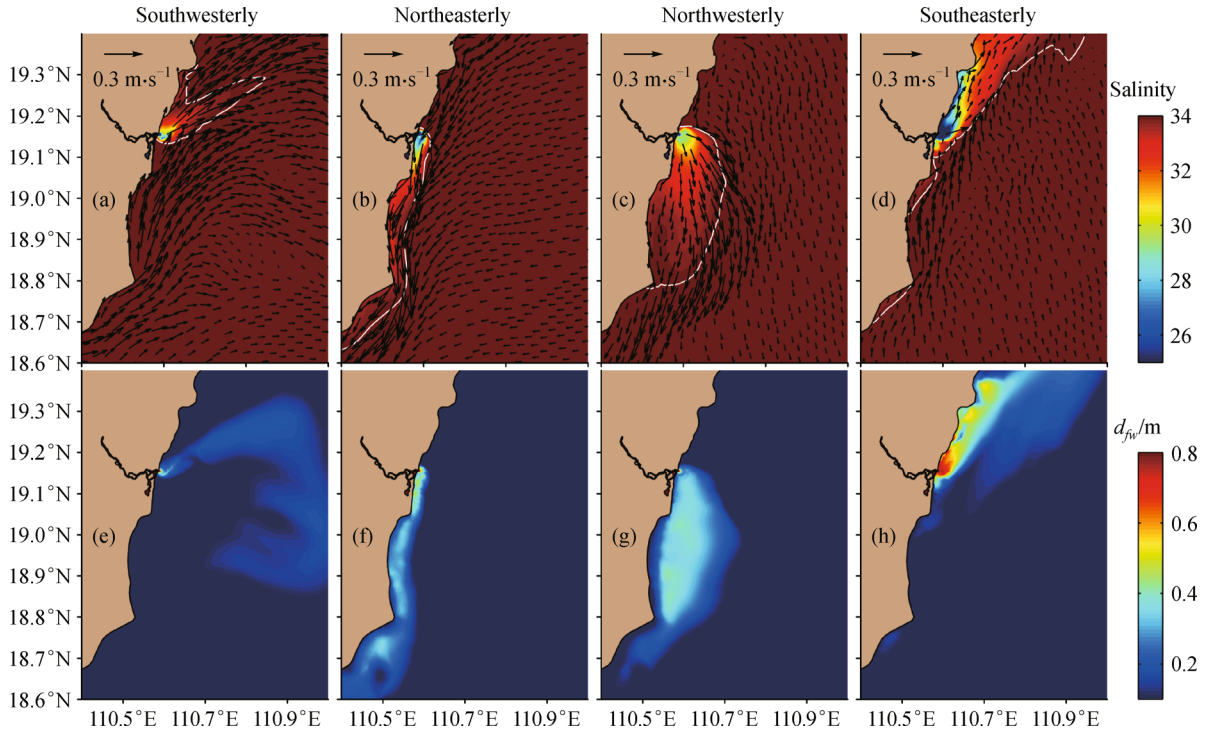

Fig. 8 The surface salinity overlain with velocity (upper panels) and freshwater depth (lower panels) after 8 days of the simulation under the 5 m·s^{-1} southwesterly (a, e), northeasterly (b, f), northwesterly (c, g), and southeasterly (d, h) winds. The white lines in the upper panel represent the 34.0-psu isohaline.

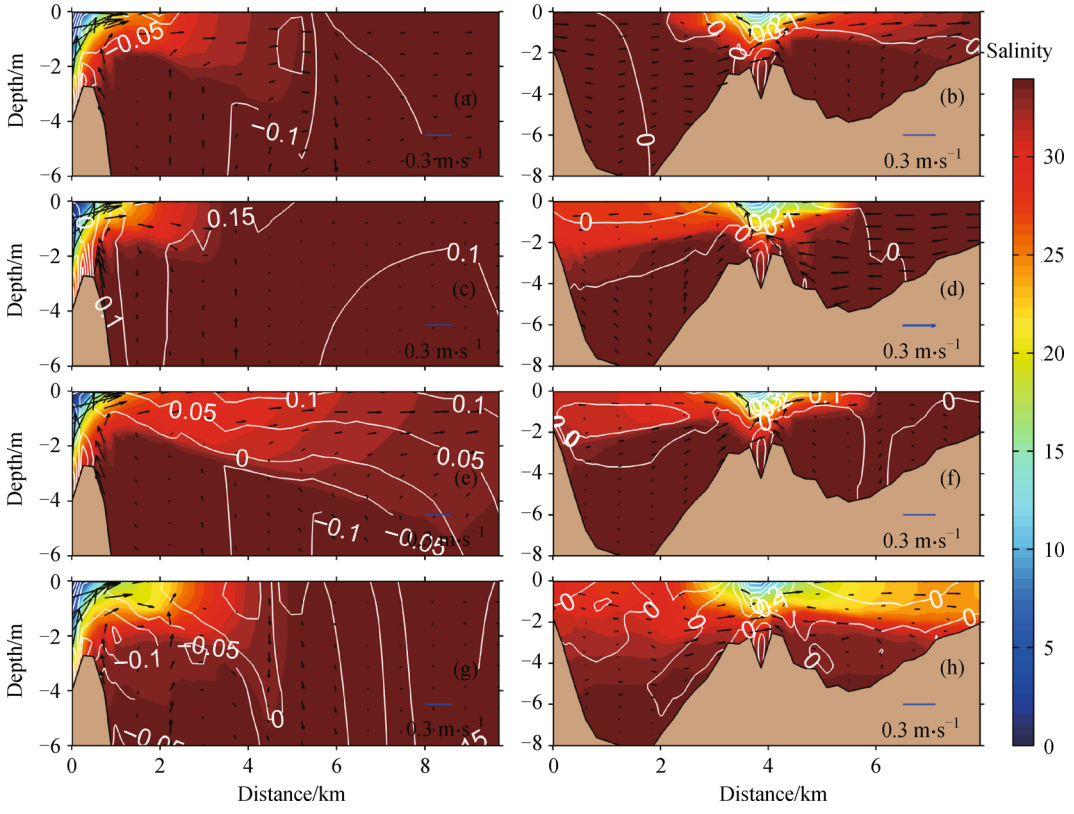

Fig. 9 The 5 m·s^{-1} wind-induced vertical salinity profile and current field for cross-shelf section (left panels) and alongshore section (right panels) after 8 days of the simulation with southwesterly (a, b), northeasterly (c, d), northwesterly (e, f), and southeasterly (g, h) winds. The distance in the cross-shelf section is from mouth to offshore, and the distance in the alongshore section is from south to north. The vertical velocity is scaled by 500 m·s^{-1}. Filled contours indicate salinity and the contours superimposed on the shading indicate alongshore velocity (in cross-shelf sections, positive down-shelf) or cross-shelf velocity (in alongshore sections, positive offshore).

side of the plume. The plume is narrow in the cross-shelf direction, stretching in the alongshore direction. The plume attaches to the floor in the up-shelf side due to the shallow water depth (Figs. 9(e) and 9(f)). From the alongshore sections, it can be seen that away from the mouth, the offshore velocity is almost zero under different wind directions. However, the two-layer cross-shelf current, with upper layer offshore and bottom layer onshore, can be observed in the cross-section for all wind conditions.

4.2.2 Effect of wind magnitude

Figure 10 shows the plume evolution under the southwesterly winds at different magnitudes. When the winds are included, less freshwater is transported down-shelf and thus decreases to a depth of less than 0.3 m away from the mouth. The plume separates from the shoreline and the freshwater is advected offshore.

When the wind is calm (Figs. 10(a) and 10(d)), the bulge structure still exists, which is similar to the base case. The bulge becomes more circular and its offshore extension increases. Less freshwater is then transported in the coastal current (~6%). Moreover, the plume in the coastal current is detached from the coastline and the salinity along the coast is higher due to the upwelling of salty water to replace the freshwater transporting offshore. When the wind speed reaches 3 $m \cdot s^{-1}$ (Figs. 10(b) and 10(e)), the bulge vanishes, and the plume turns up-shelf near the coast while turning southeast in the offshore area. The flow is in the downwind direction near the shore and flows to the right of the wind direction in the offshore area, which is consistent with Ekman dynamics in shallow and deep waters, respectively. With the increased wind speed, vertical mixing increases and the plume size decreases. When the wind speed reaches 5 $m \cdot s^{-1}$ (Figs. 8(a) and 8(e)), the plume only spreads in the nearshore, along the coast and parallel to the wind direction. However, the distribution of freshwater depth is not appreciably different from the 3 $m \cdot s^{-1}$ case. When the wind speed further increases to 10 $m \cdot s^{-1}$ (Figs. 10(c) and 10(f)), a strong northeastward surface flow develops over the coast. It should be noted that the southwesterly wind is not exactly parallel to the coastline in our study site, but rather there is a significant offshore component. The offshore component could affect the plume (Jurisa and Chant, 2013). Due to the offshore wind forcing, the plume is not against the coast. The northeast direction of freshwater advection is nearly the same direction as the wind. In the offshore area, a freshwater patch is formed at 19.05°–19.25°N and 110.8°–110.95°E due to the shedding effect (Yankovsky et al., 2001; Garcia-Berdeal et al., 2002). When the wind magnitude is $\geqslant 3$ $m \cdot s^{-1}$, part or all of the freshwater initially stored in the bulge is transported offshore 8 days later. The subsequent freshwater outflow is stored in the up-shelf side near the coast.

Along with the changes in the horizontal dispersal of the

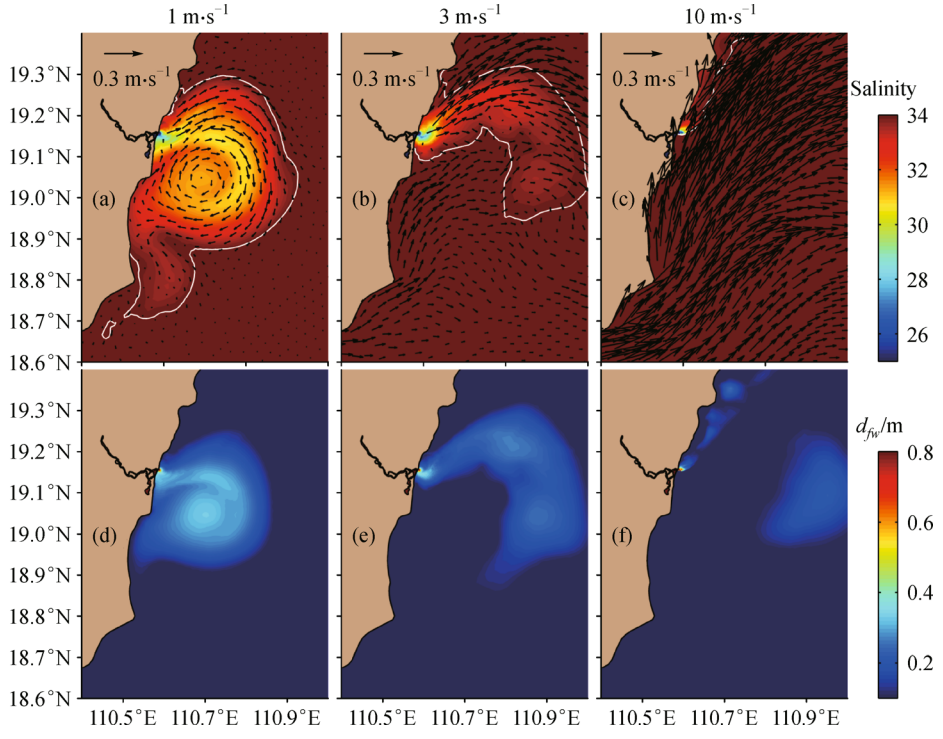

Fig. 10 The surface salinity overlain with velocity (upper panels) and freshwater depth (lower panels) after 8 days of the simulation under a southwesterly wind with 1 (a, d), 3 (b, e), and 10 $m \cdot s^{-1}$ (c, f) of speed. The corresponding results with 5 $m \cdot s^{-1}$ are shown in Figs. 8 (a) and 8(e).

plume, the vertical distributions of the current and salinity across- and along-shore change accordingly. Figure 11 compares the current and salinity in two transects under different magnitudes of the southwesterly wind. The currents and plume structures near the mouth are almost the same as the 5 $m \cdot s^{-1}$ case, except for the 10 $m \cdot s^{-1}$ case. Under the 10 $m \cdot s^{-1}$ wind, the currents at the mouth are offshore in the water column, and the undercurrent disappears. In the meantime, the plume becomes attached to the floor (Fig. 11(h)). It can be seen that the plume profile is almost the same as that of the no-wind case when the wind is weak (Figs. 11(a)–11(d)), suggesting a small wind mixing effect. When the wind is weak, the isohaline tilts nearshore, while it flattens at about 1.5 km offshore of the mouth. The depth of the plume is approximately 2 m. When the wind is 3 $m \cdot s^{-1}$ (Figs. 11(e) and 11(f)), the plume dispersal is shortened in the offshore direction, while the plume depth increases, and the stratification decreases offshore. More freshwater is transported to the up-shelf along the coast. With the wind further increased (Figs. 9(a) and 9(b)), the offshore distance of the plume shrinks, and the isohaline becomes fully vertical. Except for the outflow near the mouth, all currents are directed up-shelf. The 10 $m \cdot s^{-1}$ wind forces a large mix in the plume, spreading it less than 2 km offshore and 500 m down-shelf of the mouth. As the offshore spreading is limited, the plume water occupies the entire water column. Most of the freshwater is transported towards the up-shelf direction (Figs. 11(g) and 11(h)).

5 Freshwater flux decomposition

To investigate the influence of wind direction on the transport, the model results with a wind speed of 5 $m \cdot s^{-1}$ from the southwest, northeast, northwest, and southeast, respectively, are analyzed. As shown in Fig. 12, the wind direction has a prominent effect on the freshwater transport.

The total freshwater transport is alongshore and near the coast under the northeasterly and southeasterly winds, from opposite directions (Figs. 12(b) and 12(d)). The southwesterly and northwesterly winds transport freshwater further offshore. The oscillatory transport is very small in all cases (Figs. 12(m), 12(n), 12(o) and 12(p)). Under the southwesterly wind (Figs. 12(a), 12(e) and

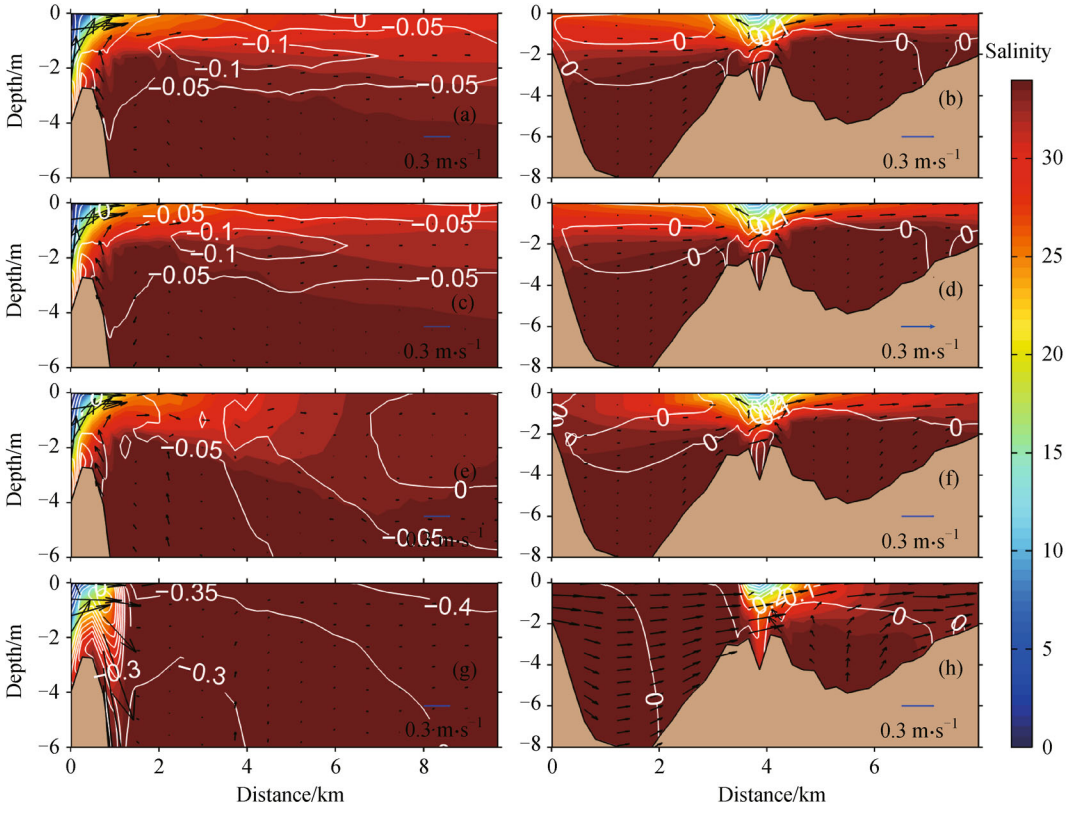

Fig. 11 The southwesterly wind-induced vertical salinity profiles and current field for the cross-shelf section (left panels) and alongshore section (right panels) after 8 days of the simulation with no wind (a, b), 1 $m \cdot s^{-1}$ (c, d), 3 $m \cdot s^{-1}$ (e, f), and 10 $m \cdot s^{-1}$ (g, h) wind speed. The corresponding results with 5 $m \cdot s^{-1}$ are shown in Figs. 9(a) and 9(b). The distance in the cross-shelf section is from the mouth to offshore, and the distance in the alongshore section is from the south to the north. The vertical velocity is scaled by 500 $m \cdot s^{-1}$. Filled contours indicate salinity and the contours superimposed on the shading indicate alongshore velocity (in cross-shelf sections, positive down-shelf) or cross-shelf velocity (in alongshore sections, positive offshore).

12(i)), the freshwater is transported towards the northeast and offshore. The advection and vertical shear are both important, but the effects are different. The advection drives the freshwater northward along the coast, while the vertical shear flux is along the freshwater flow out of the mouth, spreading offshore. When the wind is northeasterly (Figs. 12(b), 12(f), 12(j)), the freshwater is driven to the south, along the coastline. The advection is dominant down-shelf of the mouth, while the vertical shear is of more significance near the mouth. The pattern is remarkably different with a northwesterly wind (Figs. 12 (c), 12(g), and 12(k) when an anticyclonic eddy develops down-shelf of the mouth. Before the eddy turns towards the coast, the water underneath the plume flows opposite to that on the surface. As a result, a two-layer flow develops, resulting in the dominance of the vertical shear. As the eddy reaches the coastline, the separated flows are unidirectional near the surface and bottom. Consequently, the advection becomes more dominant. When the wind is southeasterly (Figs. 12(d), 12(h), and 12(l)), the freshwater is transported towards the northeast due to the Ekman effect. Both advection and the vertical shear are of importance.

The evolution of the plume under the southwesterly

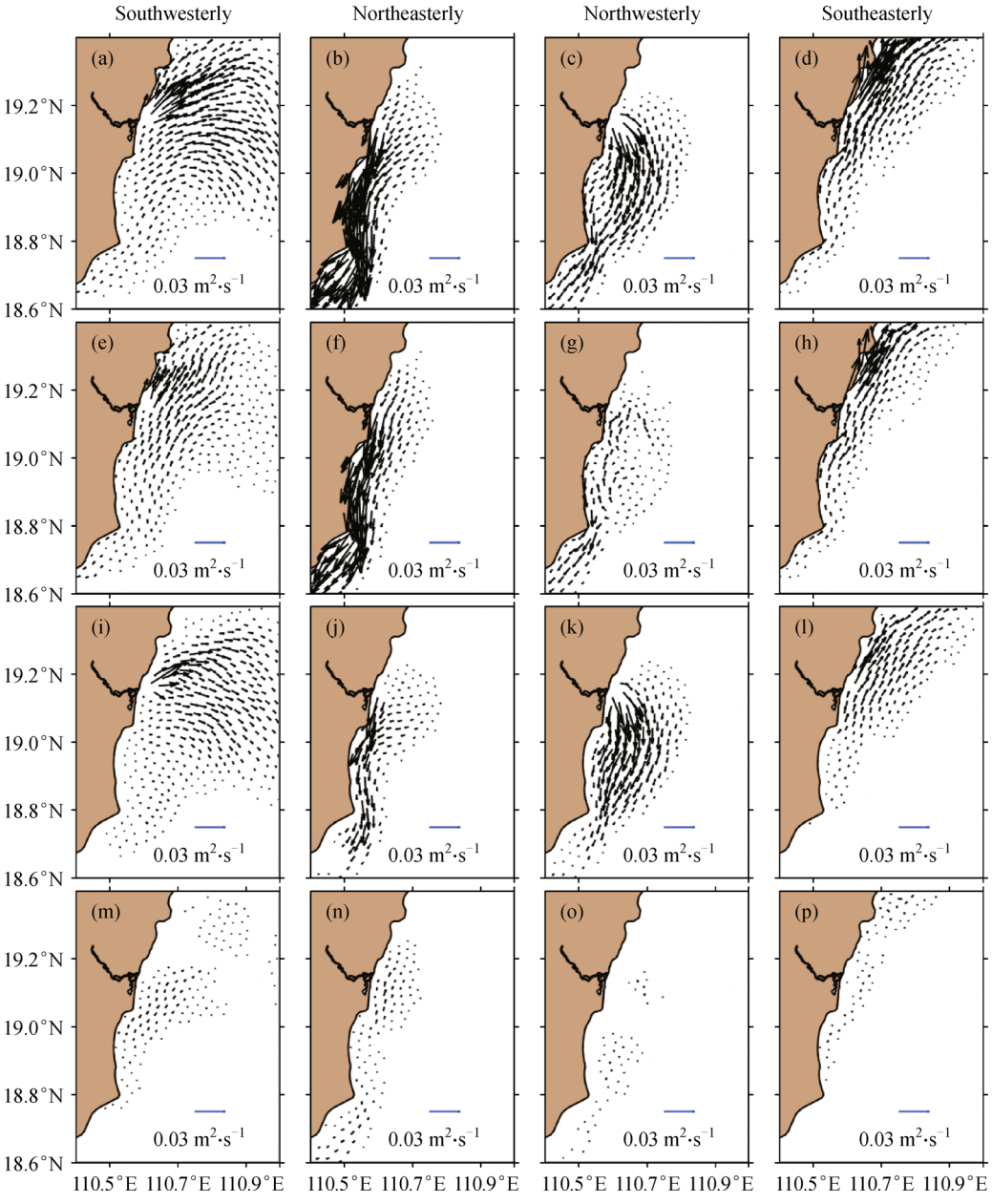

Fig. 12 Vertical integrated freshwater transport under 5 $m \cdot s^{-1}$ wind in southwesterly (a, e, i, m), northeasterly (b, f, j, n), northwesterly (c, g, k, o) and southeasterly (d, h, l, p) directions. The panels in the first, second, third, and fourth rows are total freshwater flux, the advection transport, vertical shear transport, and oscillatory transport, respectively.

winds of different magnitude is also examined (Fig. 13). The transport due to advection and shear-induced transport are comparable, while the oscillatory transport is extremely weak except when the southwesterly wind is 10 $m \cdot s^{-1}$. When the wind is weak (< 3 $m \cdot s^{-1}$) (Figs. 13(a), 13(e), 13(i), 13(b), 13(f), and 13(j)), the flow jets out of the mouth, forming an anticyclonic eddy. Along the outflow and the offshore of the eddy, the vertical shear flux is dominant, while the advection flux induces a northward transport on the coastal side. When the wind is 3 $m \cdot s^{-1}$ (Figs. 13(c), 13(g), and 13(k)), the advection flux is enhanced. The plume spreads to a larger extent and the anticyclonic eddy formed down-shelf disappears. Meanwhile, the vertical shear flux is reduced due to the increased vertical mixing. With the further increase of wind forcing (Figs. 12(a), 12(e), and 12(i)), the advection flux becomes more dominant, and the vertical shear becomes weaker. When the wind is 10 $m \cdot s^{-1}$ (Figs. 13(d), 13(h), and 13(l)), the advection dominates the transport of freshwater and drives it northward. The transition from the shear-dominant transport to the advection-dominant transport occurs at a wind speed of approximately 5 $m \cdot s^{-1}$.

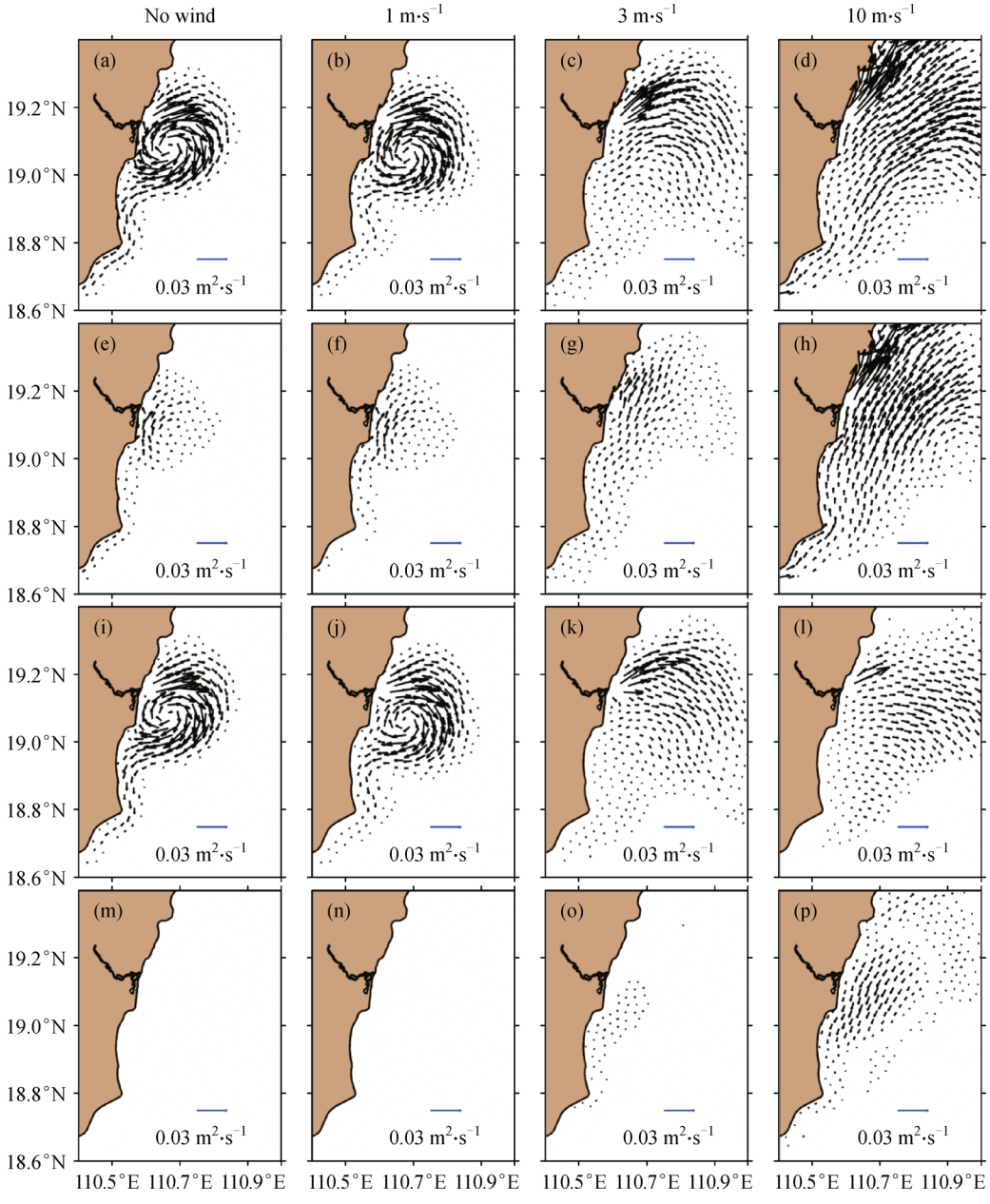

Fig. 13 Vertically integrated freshwater transport under no-wind (a, e, i, m), 1 $m \cdot s^{-1}$ (b, f, j, n), 3 $m \cdot s^{-1}$ (c, g, k, o), and 10 $m \cdot s^{-1}$ (d, h, l, p) under a southwesterly wind. The panels in the first, second, third, and fourth rows are total freshwater flux, the advection transport, vertical shear transport, and oscillatory transport, respectively. The corresponding results with 5 $m \cdot s^{-1}$ are shown in Figs. 12(a), 12(e), 12(i), 12(m).

6 Discussion

6.1 Wind forcing vs. buoyancy

In the previous sections, it is shown that in the absence of wind forcing or under light winds, the buoyancy plume propagates down-shelf due to the Coriolis force and the difference in density between the ambient water and the plume. The plume becomes more influenced as the wind stress increases. Here, we use the Wedderburn number (W) to examine the effect of the magnitude of an upwelling-favorable wind on the plume. This number has been used to examine the influence of wind on estuarine structure and circulation (Geyer, 1997; Chen and Sanford, 2009) and on the river plume (Jurisa and Chant, 2012; Dzwonkowski et al., 2015). It shows the non-dimensional ratio for the relative strength of the wind and buoyancy forcing acting on the river plume, which can be defined as

$$W = \frac{\tau_w L}{\Delta\rho g h^2}, \tag{7}$$

where τ_w is the wind stress, L is the distance from the mouth to the offshore boundary of the plume, $\Delta\rho$ is the density change over L, and g is the gravitational acceleration. When $W > 1$, the plume is dominated by the wind forcing, which can significantly modify the plume's flow and stratification. When $W < 1$, buoyancy driven dynamics control the plume structure. The results are presented in Table 2.

Table 2 Wedderburn number under different wind velocity

Wind velocity/(m·s^{-1})	Whole	Section		
		Down-shelf	Up-shelf	Offshore
1	0.02	0.01	0.02	0.03
3	0.19	0.12	0.26	0.31
5	0.54	0.34	0.71	0.85
10	2.15	1.35	2.84	3.39

It is shown that when the southwesterly wind is $\leqslant 5$ m·s^{-1}, the plume is buoyancy-controlled, while when it is 10 m·s^{-1}, wind dominates the plume. A transition threshold is when W is ~1 with a wind magnitude of 6.8 m·s^{-1}.

Furthermore, we calculate W at three sections (the locations of three sections are indicated in Fig. 7), with L being the distance from the mouth to the sections, $\Delta\rho$ the density difference between the sections and the mouth, and h the section-averaged plume depth. The results indicate that W is smallest at the down-shelf section and largest at the offshore section, suggesting that to overcome the baroclinic gradient, a stronger wind is needed down-shelf rather than up-shelf.

6.2 Wind straining vs. wind mixing

Wind can influence the freshwater transport by altering the water stratification and vertical velocity shear. If the stratification increases, the advection transport decreases, and the vertical shear transport is enhanced, and vice versa.

As stated by Whitney and Garvine (2005) and Li and Li (2011), along-shelf winds can modify the cross-shelf structure of a buoyant outflow in addition to influencing the along-shelf coastal current. These winds generate across-shelf flow through Ekman dynamics, even though the across-shelf velocities are small relative to wind-induced, along-shelf flow. Along-shelf winds act to strain a coastal current's density field through across-shelf Ekman transport.

The effect of wind straining and mixing on the plume is shown in Fig. 14. In the figure, the red color illustrates the effect of wind straining and plus (+) denotes an increase in stratification, while the black color illustrates the effect of wind mixing and minus (–) denotes a decrease in stratification. When there is no wind, the buoyancy-driven surface flow at the plume boundary are down-shelf in the coastal current, up-shelf at the up-shelf side, and offshore at the offshore side, with bottom flows in the reverse directions, as shown by the arrows in the figure. Due to the difference between wind direction and buoyant outflow, the stratifications vary in different areas of the plume. When a southwesterly wind is observed in the plume (Fig. 14(a)), the wind direction is opposite to the direction of the coastal current down-shelf of the mouth, thus the wind straining induces a destratification effect, which can be seen from the red minus sign in the down-shelf area. Associated with the wind mixing (black minus sign in the down-shelf area), the net effect of the southwesterly wind is the reduction of the stratification down-shelf of the mouth, thus reducing the vertical shear transport and increasing the advection transport. However, in the up-shelf and offshore sections of the plume, the wind straining tends to increase the stratification (red plus signs in the up-shelf and offshore parts), and the net effect of the wind is the competition between the wind straining and mixing. The northeasterly (Fig. 14(b)), northwesterly (Fig. 14(c)), and southeasterly (Fig. 14(d)) winds have similar effects.

The effects of wind on the stratification can be estimated by comparing the potential energy anomalies (PEA) with and without wind. PEA is the potential energy needed to completely mix the water column in the vertical (Simpson et al., 1981; Whitney and Garvine, 2005). Thus, the more stratified water means higher PEA. The PEA is defined as

$$\phi = \frac{1}{h}\int_{-h}^{0}(\overline{\rho}-\rho)gz\mathrm{d}z, \tag{8}$$

where $\overline{\rho}$ is the vertical averaged water density. We calculate the section-averaged PEA in different areas of the plume

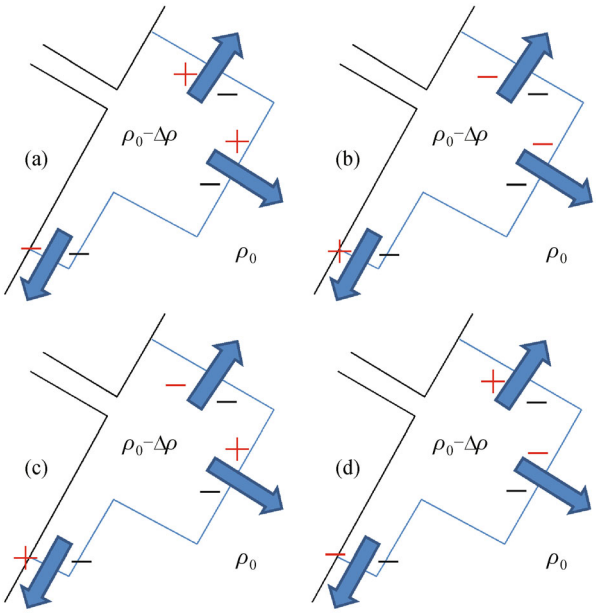

Fig. 14 Schematic diagrams showing the influence of the wind straining and mixing on the stratification of the plume under the southwesterly (a), northeasterly (b), northwesterly (c), and southeasterly (d) winds at a speed of 5 $m \cdot s^{-1}$. Arrows indicate the directions of buoyancy-driven surface flows in different areas of the plume. Symbols at two sides of the arrows indicate the effect of wind straining (red) and wind mixing (black). Plus (+) indicates an increase in stratification and minus (–) indicates a decrease.

(the locations of three sections are indicated in Fig. 7) to identify the variation of stratification under different wind conditions. PEAs under different wind forcings are further non-dimensionalized by that of the base case. If the non-dimensional PEA in a section is larger than the unity, this suggests that the wind straining is stronger than the wind mixing. The net effect of the wind is to enhance the stratification of the section, while a non-dimensional PEA smaller than unity suggests that wind mixing is dominant.

Table 3 shows that the PEA is smaller than that of the base condition in each section, except the up-shelf section when the wind is 3 $m \cdot s^{-1}$, and the up-shelf and offshore section when the wind is $\leqslant 3$ $m \cdot s^{-1}$, indicating decreased stratification under wind forcing. The decreased stratification in the sections corresponds to decreased vertical shear transport, and vice versa (Fig. 13). In general, the vertical shear transport decreases for all wind magnitudes in the down-shelf section and for up-shelf and offshore sections with winds > 3 $m \cdot s^{-1}$. When the wind is 5 $m \cdot s^{-1}$, winds from all directions decrease the stratification at the 3 sections. This can be seen from Fig. 12, where the vertical shear transports at the three sections decrease when compared with the base condition.

By comparing the PEA with W under the southwesterly wind (Fig. 15), it is found that the stratification is smaller than that of the base condition for all wind magnitudes in the down-shelf section. In the up-shelf and offshore sections, the stratifications decrease when W exceeds 0.6 and 0.7, respectively. This shows that the critical W for the transition from straining dominance to mixing dominance varies in different sections.

Table 3 Non-dimensional PEA at different parts of the plume in different wind conditions. The positions of the sections are indicated in Fig. 7

Wind	Sections		
	Down-Shelf	Up-Shelf	Offshore
0	1.00	1.00	1.00
SW-1	0.66	0.85	1.74
SW-3	0.06	1.49	1.31
SW-5	0.02	0.81	0.82
SW-10	0.01	0.08	0.42
NE-5	0.29	0.00	0.00
NW-5	0.53	0.01	0.14
SE-5	0.12	0.97	0.05

6.3 The sensitivity of the plume to tidal forcing

According to Vic et al. (2014), the tides have a negligible effect on the near-field plume dynamics when the scaled tidal amplitude (the ratio of tidal amplitude to the mouth depth) is much smaller than the unity. Whitney and Garvine (2006) and Xia et al. (2011) pointed out that tidal mixing plays a crucial role in the physical transport within the estuary and immediately outside the mouth. Tarya et al. (2015) showed that the tides generate horizontal and vertical mixing and suppress the cross-shelf dispersal in the coastal area, while the spreading of the river plume on the shelf is mainly controlled by the weak wind. By studying the barotropic circulation along the Berau continental shelf, Tarya et al. (2010) revealed that tides are dominant in the generation of mean residual currents. In our study site, the ratio of tidal amplitude (0.5 m) to mouth depth (3.4 m) is about 0.15, which is much smaller than 1, indicating that the tides can be neglected in the near-field plume dynamics.

To further estimate the tidal effect on the plume, we conducted additional experiments with and without tides. The results are shown in Fig. 16. When tides are withdrawn, the core region of the plume (salinity less than 28) is a little smaller than that with tides. Inclusion of the tides enhances the ebb flow and expands the plume. However, the plume structure with or without tides is very similar, showing that the tidal effect is insignificant in our case. This justifies our focus on the wind effect in the Wanquan River plume.

6.4 The Effect of topography on the plume

Tarya et al. (2015) have shown that the topography of the

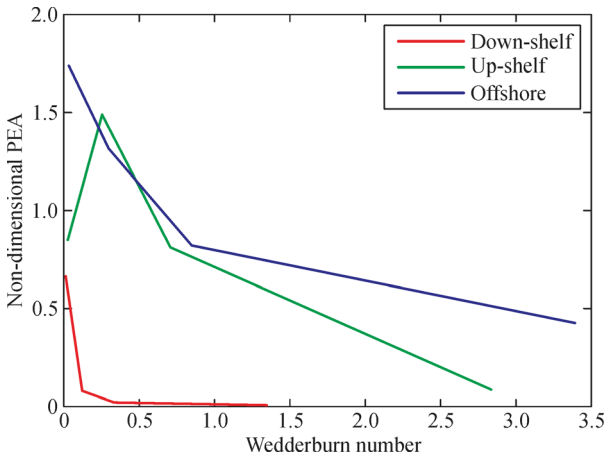

Fig. 15 The correlation between Wedderburn number and non-dimensional PEA.

Berau continental shelf has a pronounced effect on the river plume dispersal. This effect is also evident in our study area. In our case, when the plume spreads along the coast, the freshwater depth is greater in the up-shelf section than that in the down-shelf section (Figs. 9(f) and 9(h)). This is due to the asymmetry of the bathymetry up-shelf and down-shelf of the mouth. In the up-shelf area of the mouth, the shallow water region of 10 m is relatively wider compared to the shallow region in the down-shelf area of the shelf (see Fig. 1(b)). The shallower up-shelf area of the mouth enhances mixing induced by bottom turbulence and surface wind, reduces the vertical stratification, and increases surface salinity. However, it also decreases plume dispersion along the up-shelf. The situation reverses down-shelf of the mouth, where the plume is elongated as it spreads.

7 Conclusions

The variations of plume dispersion and transport of freshwater under different wind directions and magnitudes are studied for a tropical small river plume. The FVCOM model is utilized and validated against the observation data. A series of numerical experiments are conducted to investigate the wind effect. The results show that the plume dispersion and the transport of freshwater are sensitive to both wind direction and magnitude.

In the no-wind case, Wanquan River plume has the dynamical constraints of a small Kelvin number, a small Rossby number, and an internal Froude number of order 1. Thus, the outflow is jet-like and the velocity is large. A large circular bulge exists off the mouth and accumulates ~75% of the freshwater discharge, which causes a reduction of freshwater in the coastal current away from the mouth.

For a moderate wind (5 $m \cdot s^{-1}$), the southwesterly wind causes the plume to extend towards the northeast and separate from the coast. When the wind is northeasterly, the plume is confined in a narrow coastal current down-shelf of the mouth. Under the northwesterly wind, the plume is pushed down-shelf of the mouth and generates a stratified water column. The southeasterly wind drives the river plume to the northeast alongshore and the mixing is enhanced due to the shallow water depth. The total freshwater transport is alongshore and near the coast for northeasterly and southeasterly winds, forced in opposite directions. Southwesterly and northwesterly winds transport freshwater in an offshore direction. For the components of the transport, advection dominates the freshwater transport in the coastal area. The main contributor is vertical shear in the offshore area.

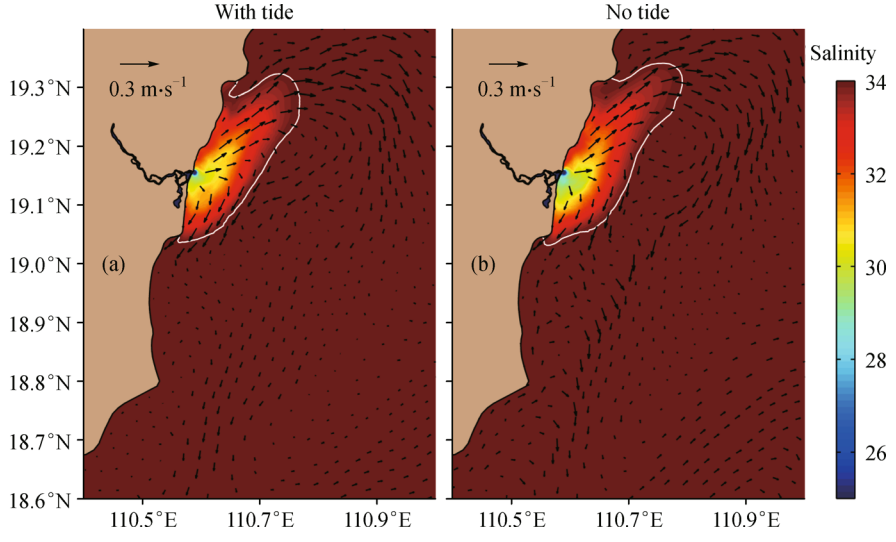

Fig. 16 Simulated surface plume and current structures on 24 August 2012 under real (a) and no-tide (b) conditions. The white lines represent the 34.0-psu isohaline.

A weak southwesterly wind acts on the plume in the form of offshore advection, while the mixing induced by the wind is weak. With increased wind stress, the mixing and associated plume depth increases, while the plume size and offshore dispersal decreases. The freshwater is pushed towards the northeast and is then forced in the offshore direction. This suggests that the plume dispersal is primarily controlled by the wind-induced current in the plume near-field, while the Coriolis force is more dominant in the plume far-field. With increased wind stress, the freshwater transport is more dependent on the advection transport due to increased vertical mixing.

The calculated Wedderburn number indicates that when the wind exceeds 6.8 $m \cdot s^{-1}$, the plume is dominated by wind forcing. However, in other sections of the plume, the importance of the wind forcing is different due to the different baroclinic pressure gradient. The wind is of more significance in the up-shelf and offshore areas of the plume than in the down-shelf areas. The stratification of the plume decreases under the southwesterly wind, except in the up-shelf and offshore areas where wind speeds are lower.

Acknowledgements This study is funded by the National Natural Science Foundation of China (Grant No. 40976052). This research is supported in part by Special Program for Applied Research on Super Computation of the NSFC-Guangdong Joint Fund (the second phase). The authors would like to acknowledge Mr. Mac Sisson of Virginia Institute of Marine Science for his help in editing the manuscript. We are also grateful for the three anonymous reviewers for helpful comments on the manuscript.

References

Avicola G, Huq P (2003). The role of outflow geometry in the formation of the recirculating bulge region in coastal buoyant outflows. J Mar Res, 61(4): 411–434

Bourrin F, Friend P L, Amos C L, Manca E, Ulses C, Palanques A, Durrieu de Madron X, Thompson C E L (2008). Sediment dispersal from a typical Mediterranean flood: the Têt River, Gulf of Lions. Cont Shelf Res, 28(15): 1895–1910

Chao S Y (1988a). River-forced estuarine plumes. J Phys Oceanogr, 18 (1): 72–88

Chao S Y (1988b). Wind-driven motion of estuarine plumes. J Phys Oceanogr, 18(8): 1144–1166

Chao S Y (1990). Tidal modulation of estuarine plumes. J Phys Oceanogr, 20(7): 1115–1123

Chen C S, Liu H D, Beardsley R C (2003). An unstructured grid, finite-volume, three-dimensional, primitive equations ocean model: application to coastal ocean and estuaries. J Atmos Ocean Technol, 20(1): 159–186

Chen C S, Xue P F, Ding P X, Beardsley R C, Xu Q C, Mao X M, Gao G P, Qi J H, Li C Y, Lin H C, Cowles G, Shi M C (2008). Physical mechanisms for the offshore detachment of the Changjiang diluted water in the East China Sea. Journal of Geophysical Research: Oceans, 113(C2): C02002

Chen S N, Sanford L P (2009). Axial wind effects on stratification and longitudinal salt transport in an idealized, partially mixed estuary. J Phys Oceanogr, 39(8): 1905–1920

Choi B J, Wilkin J L (2007). The effect of wind on the dispersal of the Hudson River plume. J Phys Oceanogr, 37(7): 1878–1897

Dzwonkowski B, Park K, Collini R (2015). The coupled estuarine-shelf response of a river-dominated system during the transition from low to high discharge. Journal of Geophysical Research: Oceans, 120(9): 6145–6163

Egbert G D, Erofeeva S Y (2002). Efficient inverse modeling of Barotropic Ocean Tides. J Atmos Ocean Technol, 19(2): 183–204

Fong D A, Geyer W R (2001). Response of a river plume during an upwelling favorable wind event. Journal of Geophysical Research: Oceans, 106(C1): 1067–1084

Fong D A, Geyer W R (2002). The alongshore transport of freshwater in a surface-trapped river plume. J Phys Oceanogr, 32(3): 957–972

Fong D A, Geyer W R, Signell R P (1997). The wind-forced response on a buoyant coastal current: observations of the western Gulf of Maine plume. J Mar Syst, 12(1–4): 69–81

García-Berdeal I, Hickey B, Kawase M (2002). Influence of wind stress and ambient flow on a high discharge river plume. J Geophys Res, 107(C9): 3130

Garvine R W (1995). A dynamical system for classifying buoyant coastal discharges. Cont Shelf Res, 15(13): 1585–1596

Garvine R W (1999). Penetration of buoyant coastal discharge onto the continental shelf: a numerical model experiment. J Phys Oceanogr, 29(8): 1892–1909

Gaston T F, Schlacher T A, Connolly R M (2006). Flood discharges of a small river into open coastal waters: plume traits and material fate. Estuar Coast Shelf Sci, 69(1–2): 4–9

Ge J Z, Ding P X, Chen C S (2015). Low-salinity plume detachment under non-uniform summer wind off the Changjiang Estuary. Estuar Coast Shelf Sci, 156: 61–70

Geyer W R (1997). Influence of wind on dynamics and flushing of shallow estuaries. Estuar Coast Shelf Sci, 44(6): 713–722

Geyer W R, Hill P, Milligan T, Traykovski P (2000). The structure of the Eel River plume during floods. Cont Shelf Res, 20(16): 2067–2093

Geyer W R, Hill P S, Kineke G C (2004). The transport, transformation and dispersal of sediment by buoyant coastal flows. Cont Shelf Res, 24(7–8): 927–949

Guo X Y, Valle-Levinson A (2007). Tidal effects on estuarine circulation and outflow plume in the Chesapeake Bay. Cont Shelf Res, 27(1): 20–42

Hetland R D (2005). Relating river plume structure to vertical mixing. J Phys Oceanogr, 35(9): 1667–1688

Horner-Devine A R, Fong D A, Monismith S G, Maxworthy T (2006). Laboratory experiments simulating a coastal river inflow. J Fluid Mech, 555: 203–232

Huq P (2009). The role of Kelvin number on Bulge formation from estuarine buoyant outflows. Estuaries Coasts, 32(4): 709–719

Isobe A (2005). Ballooning of river-plume bulge and its stabilization by tidal currents. J Phys Oceanogr, 35(12): 2337–2351

Johnson D, Weidemann A, Arnone R, Davis C (2001). Chesapeake Bay outflow plume and coastal upwelling events: physical and optical properties. J Geophys Res, 106(C6): 11613–11622

Jurisa J T, Chant R (2012). The coupled Hudson River estuarine-plume response to variable wind and river forcings. Ocean Dyn, 62(5): 771–

784

Jurisa J T, Chant R J (2013). Impact of offshore winds on a buoyant river plume system. J Phys Oceanogr, 43(12): 2571–2587

Large W, Pond S (1981). Open ocean momentum flux measurements in moderate to strong winds. J Phys Oceanogr, 11(3): 324–336

Lentz S J, Largier J (2006). The influence of wind forcing on the Chesapeake Bay buoyant coastal current. J Phys Oceanogr, 36(7): 1305–1316

Li Y, Li M (2011). Effects of winds on stratification and circulation in a partially mixed estuary. J Geophys Res, 116(C12): 12012

Moffat C, Lentz S (2012). On the response of a buoyant plume to downwelling-favorable wind stress. J Phys Oceanogr, 42(7): 1083–1098

Nof D, Pichevin T (2001). The ballooning of outflows. J Phys Oceanogr, 31(10): 3045–3058

Ostrander C E, McManus M A, DeCarlo E H, Mackenzie F T (2008). Temporal and spatial variability of freshwater plumes in a semienclosed estuarine–bay system. Estuaries Coasts, 31(1): 192–203

Pan J Y, Gu Y Z, Wang D X (2014). Observations and numerical modeling of the Pearl River plume in summer season. Journal of Geophysical Research: Oceans, 119(4): 2480–2500

Piñones A, Valle-Levinson A, Narváez D A, Vargas C A, Navarrete S A, Yuras G, Castilla J C (2005). Wind-induced diurnal variability in river plume motion. Estuar Coast Shelf Sci, 65(3): 513–525

Rabalais N N, Turner R E, Wiseman W J Jr (2002). Gulf of Mexico hypoxia, aka "The dead zone". Annu Rev Ecol Syst, 33(1): 235–263

Ralston D K, Geyer W R, Lerczak J A (2010). Structure, variability, and salt flux in a strongly forced salt wedge estuary. Journal of Geophysical Research: Oceans, 115(C6):160–164

Rennie S E, Largier J L, Lentz S J (1999). Observations of a pulsed buoyancy current downstream of Chesapeake Bay. J Geophys Res, 104(C8): 18227–18240

Saha S, Moorthi S, Wu X, Wang J, Nadiga S, Tripp P, Behringer D, Hou Y T, Chuang H y, Iredell M, Ek M, Meng J, Yang R, Mendez M P, van den Dool H, Zhang Q, Wang W, Chen M, Becker E (2014). The NCEP Climate Forecast System Version 2. J Clim, 27(6): 2185–2208

Sanders T M, Garvine R W (2001). Fresh water delivery to the continental shelf and subsequent mixing: an observational study. J Geophys Res, 106(C11): 27087–27101

Shu Y Q, Chen J, Yao J L, Pan J Y, Wang W W, Mao H B, Wang D X (2014). Effects of the Pearl River plume on the vertical structure of coastal currents in the Northern South China Sea during summer 2008. Ocean Dyn, 64(12): 1743–1752

Shu Y Q, Wang D X, Zhu J A, Peng S Q (2011). The 4-D structure of upwelling and Pearl River plume in the northern South China Sea during summer 2008 revealed by a data assimilation model. Ocean Model, 36(3–4): 228–241

Simpson J (1997). Physical processes in the ROFI regime. J Mar Syst, 12 (1): 3–15

Simpson J H, Crisp D J, Hearn C (1981). The shelf-sea fronts: implications of their existence and behaviour. Philos Trans R Soc Lond A, 302(1472): 531–546 (and Discussion)

Tarya A, Hoitink A J F, Van der Vegt M (2010). Tidal and subtidal flow patterns on a tropical continental shelf semi-insulated by coral reefs. Journal of Geophysical Research: Oceans, 115(C9): C09029

Tarya A, van der Vegt M, Hoitink A J F (2015). Wind forcing controls on river plume spreading on a tropical continental shelf. Journal of Geophysical Research: Oceans, 120(1): 16–35

Vic C, Berger H, Treguier A M, Couvelard X (2014). Dynamics of an equatorial river plume: theory and numerical experiments applied to the congo plume case. J Phys Oceanogr, 44(3): 980–994

Wang J H, Shen Y M, Guo Y K (2010). Seasonal circulation and influence factors of the Bohai Sea: a numerical study based on Lagrangian particle tracking method. Ocean Dyn, 60(6): 1581–1596

Warner J C, Geyer W R, Lerczak J A (2005). Numerical modeling of an estuary: a comprehensive skill assessment. Journal of Geophysical Research: Oceans, 110(C5): C05001

Warrick J A, DiGiacomo P M, Weisberg S B, Nezlin N P, Mengel M, Jones B H, Ohlmann J C, Washburn L, Terrill E J, Farnsworth K L (2007). River plume patterns and dynamics within the Southern California Bight. Cont Shelf Res, 27(19): 2427–2448

Whitehead J A (1985). The deflection of a baroclinic jet by a wall in a rotating fluid. Journal of Fluid Mechanics, 157: 79–93

Whitney M M, Garvine R W (2005). Wind influence on a coastal buoyant outflow. Journal of Geophysical Research: Oceans, 110(C3): C03014

Whitney M M, Garvine R W (2006). Simulating the Delaware Bay buoyant outflow: comparison with observations. J Phys Oceanogr, 36 (1): 3–21

Wu H, Zhu J R, Shen J, Wang H (2011). Tidal modulation on the Changjiang River plume in summer. Journal of Geophysical Research: Oceans, 116: C08017

Xia M, Xie L, Pietrafesa L J, Whitney M M (2011). The ideal response of a Gulf of Mexico estuary plume to wind forcing: its connection with salt flux and a Lagrangian view. J Geophys Res, 116(C8): C08035

Yankovsky A E, Hickey B M, Munchow A K (2001). Impact of variable inflow on the dynamics of a coastal buoyant plume. J Geophys Res, 106(19): 809–819, 824

Yin K, Harrison P J, Pond S, Beamish R J (1995). Entrainment of nitrate in the Fraser River Estuary and its biological implications. II. Effects of spring vs. neap tides and river discharge. Estuar Coast Shelf Sci, 40 (5): 529–544

Zhang H, Sheng J Y (2013). Estimation of extreme sea levels over the eastern continental shelf of North America. Journal of Geophysical Research: Oceans, 118(11): 6253–6273

AUTHOR BIOGRAPHIES

Junpeng Zhao is a Ph.D candidate in Sun Yat-Sen University, Guangzhou, China. He received his Bachelor's Degree at Henan University in 2009, and his Master's Degree in physical oceanography in 2011 at Sun Yat-Sen University.

His major field of study is estuarine circulation, salt intrusion in estuaries, and river plume dynamics.

E-mail: zhaojunpeng1987@163.com

Wenping Gong is a professor in the School of Marine Science, Sun Yat-Sen University, Guangzhou, China. He received his

Bachelor's Degree and Master's Degree in natural geography in 1990 and 1993 at Nanjing University, respectively. He was awarded his Ph.D. degree in physical geography in 1997 at East China Normal University, Shanghai.

He worked in the Department of Civil Engineering, the University of Liverpool, from 2000–2001, followed by a position at the Virginia Institute of Marine Science, Virginia, USA from 2003–2008. His research interests are estuarine and coastal hydrodynamics, sediment dynamics, and water quality.

E-mail: gongwp@mail.sysu.edu.cn

Jian Shen is a Professor of physical oceanography in Virginia Institute of Marine Science, Virginia, USA. He earned his Bachelor's Degree from Shanghai Normal University, and his Master's and Ph. D. degrees inform the College of William and Mary, Virginia, USA.

He worked as a visiting scientist in The Netherlands Institute for Sea Research, The Netherlands from 1986–1987, followed by a position as a Senior Environment Engineer at Tetra Tech, Inc. after he completed his Ph.D. studies. He then returned to the Virginia Institute of Marine Science for further academic research. His research interests include: estuarine circulation, inverse modeling of estuarine water quality, storm surge and inundation predictions; numerical model simulations of hydrodynamics and water quality in estuaries and coastal sea; and numerical modeling of watershed processes.

E-mail: Shen@vims.edu